

Bachelor Thesis

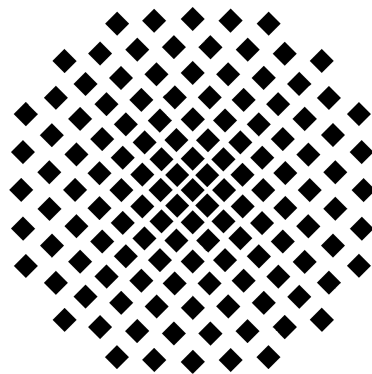
**A Photonic Crystal Cavity
Resonating With Rubidium Vapor**

by

Muamera Basic

23rd August 2018

Examiner: Prof. Dr. Tilman Pfau



5th Institute of Physics
University of Stuttgart
Pfaffenwaldring 57, 70569 Stuttgart

Ehrenwörtliche Erklärung

Hiermit versichere ich, dass ich diese Arbeit selbst verfasst habe und nur die angegebenen Quellen verwendet wurden. Alle wörtlich oder sinngemäß aus anderen Werken übernommenen Aussagen sind als solche gekennzeichnet. Die eingereichte Arbeit ist oder war weder als Ganzes, noch in wesentlichen Teilen Gegenstand eines anderen Prüfungsverfahrens und wurde weder vollständig noch in Teilen bereits veröffentlicht. Der Inhalt des gedruckten und elektronischen Exemplars stimmt überein.

Declaration of Authorship

Hereby I declare that I wrote this thesis on my own and I did not use any other sources than those referred to. Parts that are quotes or paraphrases of other works are marked as such by indicating the references. This thesis is neither whole nor partly subject of another examination and has not been published elsewhere. The electronic and printout version are identical.

Muamera Basic,
23rd August 2018

Contents

1	Introduction	3
2	Theory	5
2.1	Photonic Crystals	5
2.2	Atom-Light Interaction	11
2.3	Cavity Quantum Electrodynamics	16
3	Basics of the Simulation	19
3.1	Lumerical	19
3.1.1	The FDTD Method	19
3.1.2	Simulation Tools and Objects	20
3.1.3	A Photonic Crystal Cavity Simulation	23
3.2	Matlab	27
3.2.1	Runge-Kutta Method	27
3.2.2	Monte-Carlo Analysis	28
4	Results	31
4.1	Bandstructure	31
4.2	Bloch Modes	33
4.3	Cavity Mode Profiles	34
4.4	Cavity QED parameters	38
4.5	Temperature dependence of the PhC cavity	40
5	Outlook	43
5.1	A Two-Level Atom coupled to the PhC Cavity	43
6	Conclusion	49
	Bibliography	51

Zusammenfassung

Im Rahmen dieser Bachelorarbeit wird mithilfe eines Defekts in einem photonischen Kristall ein optischer Resonator der Resonanzwellenlänge 780 nm erzeugt. Diese Wellenlänge entspricht dem D_2 Übergang im Rubidiumatom. Zunächst wird gezeigt, welche Effekte in einem photonischen Kristall zu einer Bandlücke führen und worauf bei der Herstellung einer Cavity aus dem Kristall geachtet werden muss.

Daraufhin wird die Auswirkung des Cavity-Designs auf Größen wie den Quality-Faktor, den Purcell-Faktor und die Kooperativität der Rubidium-Atome untersucht. Abschließend wird die Rabi-Oszillation eines Rubidiumatoms im Zentrum der Cavity simuliert und ausgewertet. Die Untersuchung legt dabei nahe, dass die Atom-Licht-Wechselwirkung in der Cavity soweit gestärkt werden kann, dass die in heißen Atomen auftretenden Dekohärenzeffekte und die Flugzeitverbreiterung überwunden werden können.

Abstract

In the course of this Bachelor thesis, an optical resonator is designed in a one-dimensional photonic crystal and later optimized to support a resonance at 780 nm. This wavelength corresponds to the D_2 transition in a rubidium atom.

First, the thesis deals with the question which parameters influence which properties of photonic crystal band gaps and what has to be taken into account when designing a Cavity. Second, cavity quantum electrodynamics parameters such as the quality factor, the purcell factor and the cooperativity of rubidium atoms within the cavity are investigated. Finally, Rabi oscillations of a rubidium-atom passing through the cavity are demonstrated and the excitation states are studied. The results of this study suggest that in such a well-designed, high-Q cavity the coherent atom-light interaction is large enough to overcome the decoherence mechanisms and transit time broadening of the atoms in a thermal vapor, hence approaching the strong coupling limit in such hybrid systems.

1 Introduction

The structures of a photonic crystal (PhC) cavity offer an exceptional potential to future technological applications based on strong atom-light interaction. In fields ranging from classical to quantum information processing and nonlinear optics to compact biomedical and chemical sensing PhCs are already widely used [1].

PhCs are nano-structured, low-loss, periodic, dielectric media supporting photonic band gaps due to the periodically varying regions of high and low refractive indices. Band gaps are historically well-known from solid-state physics where the propagation of electrons is prohibited by ionic potentials in semi-conductor lattices.

In PhCs the periodic potential of an atom lattice is replaced by a potential of changing refractive indices controlling the propagation of light instead of electrons. Wavelengths allowed to pass a PhC build Bloch modes while other wavelengths are eliminated by reflections and destructive interference at lower refractive index regions causing a photonic band gap which prevents light with a frequency within the gap from propagating into a certain direction.

Depending on whether a PhC has a periodicity in one, two or three dimensions, it exhibits a one, two or three dimensional band gap. In order to create a complete band gap, i.e. preventing light with a specified frequency from propagating in every direction, a PhC lattice must be periodic along the x -, y - and z - direction [2]. Due to the difficulties in fabrication of three-dimensional PhCs, one- or two-dimensional structures are commonly used for scientific research. Moreover, the choice of a one dimensional PhC cavity is even more favorable due to its simple compatibility with laser coupling [3].

Breaking the periodicity of a PhC structure creates a defect center supporting a localized photonic mode within the photonic bandgap of the crystal. The frequency of the energy trapped between the periodic parts of the crystal is denoted as the resonance frequency. Figure 1.1 shows a schematic of a standing wave trapped in the non-periodic defect center of the PhC similar to a Bragg resonator where a standing wave is developed between the two Bragg mirrors.

Choosing the resonance wavelength of the defect center to match with a transition in an atom leads to atom-light interaction in the vicinity of PhC cavities. The PhC cavity studied in this thesis consists of silicon nitride (Si_3N_4) and is tailored to the resonance wavelength of 780.24 nm matching the D_2 transition of the rubidium

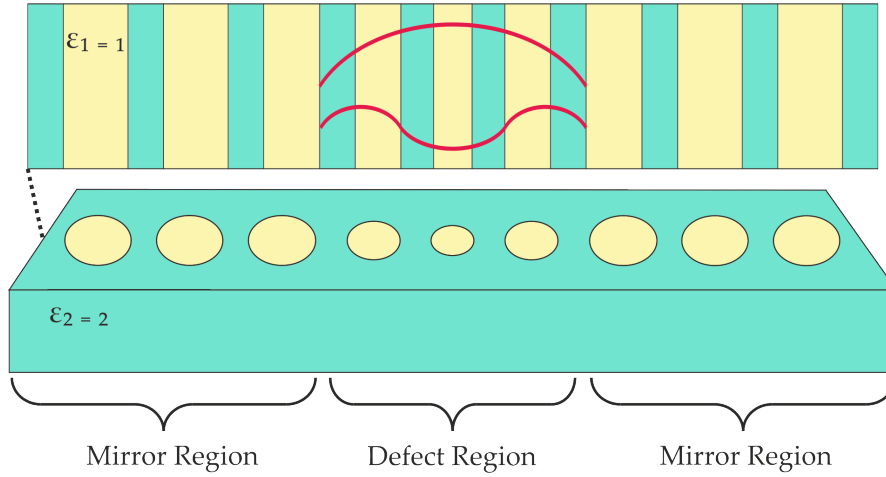


FIGURE 1.1: A Schematic of a one-dimensional PhC cavity made out of air holes (yellow, $\epsilon_1 = 1$) in a silicon nitride slab (blue, $\epsilon_2 = 2$). The mirror regions obtain a photonic band gap which is preventing light with a specified frequency from propagating in the x -direction. Breaking the periodicity of the structure in the defect region creates a localized photonic mode depicted in red within the photonic bandgap of the crystal.

atom.

An idealized, two-level rubidium atom flying in the vicinity of the cavity can undergo Rabi oscillations, i.e. absorb a cavity photon, get excited and emit the photon back into the structure where the cycle restarts again. The investigation of such Rabi cycles, i.e. the behavior of the rubidium atoms as they interact with these nano-scale cavity is one of the main goals of this thesis.

Despite the long study of photonic crystals, a design of a specific structure for a precise resonance wavelength is still challenging. Long simulation times and high sensitivity of the structures to small changes in the defect region impose an impediment of the design process. That is why the summary of the design process of the PhC cavity is another goal of this work.

The thesis begins with a theoretical description of the origin of photonic band gaps and the effects of defect centers in PhCs. It continues with the derivation of the optical Bloch equations for a two-level atom and ends with the introduction of cavity quantum electrodynamics parameters. The third chapter gives an overview of the codes and parameters set in Lumerical or Matlab for simulating the cavity and Rabi oscillations of the atom. Chapter four deals with the theoretical results of the investigated PhC cavity. Finally, a summary of the results and an outlook for the future follow up theoretical and experimental studies are given in the last chapter.

2 Theory

2.1 Photonic Crystals

This chapter aims to show the origin of band gaps in photonic crystals. The Bloch Theorem as well as the Master Equation leading to the band gap will be derived.

Bloch's Theorem

The energy gap between the valence and the conductive band for electrons in semiconductors is caused by a periodic potential of an ionic, atomic lattice $\mathbf{V}(\mathbf{r})$. This potential is assumed to have a translational symmetry

$$\mathbf{V}(\mathbf{r}) = \mathbf{V}(\mathbf{r} + \mathbf{a}) = \mathbf{V}(\mathbf{r} + n \cdot \mathbf{a}) \quad (2.1)$$

with the periodic lattice vector \mathbf{a} and the position vector \mathbf{r} . The Fourier transform of the potential is given by

$$\mathbf{V}(\mathbf{r}) = \sum_{\mathbf{G}} A_{\mathbf{G}} e^{i\mathbf{G}\mathbf{r}} \quad (2.2)$$

where \mathbf{G} is the reciprocal lattice vector [4]. When the Fourier components of the electron wave function, $\psi(\mathbf{r}) = \sum_{\mathbf{k}} C(\mathbf{k}) e^{i\mathbf{k}\mathbf{r}}$ and the potential (2.2) are plugged into Schrödinger's equation, one gets

$$\sum_{\mathbf{k}} e^{i\mathbf{k}\mathbf{r}} \left[\left(\frac{\hbar^2 \mathbf{k}^2}{2m} - E \right) C_{\mathbf{k}} + \sum_{\mathbf{G}} V_{\mathbf{G}} C_{\mathbf{k}-\mathbf{G}} \right] = 0, \quad (2.3)$$

where the term in the brackets must equal to zero. This yields a solution for the wave function as

$$\psi_{\mathbf{k}}(\mathbf{r}) = \underbrace{\sum_{\mathbf{G}} C_{\mathbf{k}-\mathbf{G}} \cdot e^{-i\mathbf{G}\mathbf{r}}}_{A_{\mathbf{k}}(\mathbf{r})} \cdot e^{i\mathbf{k}\mathbf{r}}. \quad (2.4)$$

In the above equation the underbraced term is defined as the harmonic function $A(\mathbf{r})$. This solution of the wave function is composed of a periodic envelope having

the same periodicity as the solid lattice and plane wave $e^{i\mathbf{k}\mathbf{r}}$ describing a phase factor of the propagating electron wave. In general, this solution can be applied to every wave function in a periodic lattice and is known as the Bloch theorem [5].

Instead of atomic lattices, a function of varying refractive indices in PhCs is considered as the potential for propagating light waves. With the help of Bloch's Theorem, the origin of photonic band gaps will be derived in the next sections.

Translational Symmetry and Bloch Modes

A one-dimensional PhC as the one depicted in figure 2.1 can be broken up into discrete unit cells which builds up the whole crystal through translational symmetry. This is achieved through the translation operator \mathbf{T} which translates a unit cell by the lattice constant a in the direction of the primitive lattice vector [2]. The result of a translation,

$$\mathbf{T}e^{i\mathbf{k}_x x} = e^{i\mathbf{k}_x(x-na)} = (e^{-i\mathbf{k}_x na}) e^{i\mathbf{k}_x x}, \quad (2.5)$$

shows the term $e^{i\mathbf{k}_x x}$ itself is again multiplied by some constant $e^{i\mathbf{k}_x na}$. For an eigenvalue problem, this implies that the operators $\hat{\Theta}$ and \mathbf{T} can commute and they have the same set of eigenfunctions. Inserting $|\mathbf{k}_x| = |\boldsymbol{\beta}| = 2\pi/a$ into expression (2.5) shows that the spatial propagation of the plane wave stays unchanged when replacing \mathbf{k} with the reciprocal lattice vector $\boldsymbol{\beta}$,

$$(e^{-i\mathbf{k}_x na}) e^{i\mathbf{k}_x x} \cong \underbrace{(e^{-i\boldsymbol{\beta} na})}_{\cong 1} e^{i\mathbf{k}_x x}. \quad (2.6)$$

This implies that the frequencies must also be periodic in the x -direction $\omega_{\mathbf{k}_x}(k_x) = \omega_{\mathbf{k}_x}(k_x + n\boldsymbol{\beta})$. In fact, only frequencies for k_x in the range from $-\pi/a < k_x < \pi/a$, need to be considered.

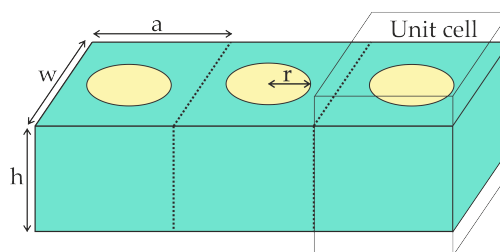


FIGURE 2.1: Schematics of a one-dimensional PhC. The whole structure is built up through a translation of the unit cells by the lattice constant a . The unit cell has a height h , width w and holes with radius r .

Origin of the Band Gap in Photonic Crystals

The propagation of electromagnetic fields is described by the macroscopic Maxwell equations. For linear, lossless dielectric materials they are given by

$$\nabla \times \mathbf{E}(\mathbf{r}, t) = -\mu_0 \frac{\partial \mathbf{H}(\mathbf{r}, t)}{\partial t}, \quad (2.7)$$

$$\nabla \times \mathbf{H}(\mathbf{r}, t) = \epsilon_0 \epsilon(\mathbf{r}) \frac{\partial \mathbf{E}(\mathbf{r}, t)}{\partial t}, \quad (2.8)$$

$$\nabla \cdot [\epsilon(\mathbf{r}) \mathbf{E}(\mathbf{r}, t)] = 0, \quad (2.9)$$

$$\nabla \cdot \mathbf{H}(\mathbf{r}, t) = 0, \quad (2.10)$$

with the electric and magnetic fields \mathbf{E} and \mathbf{H} , the vacuum permittivity $\epsilon_0 \approx 8.854 \cdot 10^{-12}$ F/m, the position-dependent relative permittivity $\epsilon(\mathbf{r})$ and the vacuum permeability $\mu_0 = 4\pi \cdot 10^{-7}$ H/m [2]. For the sake of simplicity, the problem is restricted to dielectric media with no free charges, ρ , and no free currents, \mathbf{J} . Due to the linearity of Maxwell's Equations, the time and spatial dependence can be separated from each other. Thus, expanding the fields into a set of harmonic modes,

$$\mathbf{H}(\mathbf{r}, t) = \mathbf{H}(\mathbf{r})e^{-i\omega t}, \quad \mathbf{E}(\mathbf{r}, t) = \mathbf{E}(\mathbf{r})e^{-i\omega t}, \quad (2.11)$$

with the amplitudes $\mathbf{E}(\mathbf{r})$ and $\mathbf{H}(\mathbf{r})$ provides a convenient mathematical description of the electromagnetic fields where ω is the radial frequency and t is the time [2]. As well as for the wave function of an electron, the Bloch Theorem can be applied to describe the amplitudes of the electromagnetic waves [2],

$$\mathbf{H}(\mathbf{r}) = \mathbf{H}_{\mathbf{k}}(\mathbf{r}) \cdot e^{i\mathbf{k}\mathbf{r}}, \quad \mathbf{E}(\mathbf{r}) = \mathbf{E}_{\mathbf{k}}(\mathbf{r}) \cdot e^{i\mathbf{k}\mathbf{r}}. \quad (2.12)$$

Re-writing the equations in terms of the magnetic field \mathbf{H} only and substituting Maxwell's curl equation (2.7) into (2.8) leads to the **Master Equation**

$$\underbrace{(\nabla + i\mathbf{k}) \times \frac{1}{\epsilon_r} (\nabla + i\mathbf{k}) \times}_{=\hat{\Theta}} \mathbf{H}_{\mathbf{k}} = \left(\frac{\omega_{\mathbf{k}}}{c_0} \right)^2 \mathbf{H}_{\mathbf{k}} \quad (2.13)$$

with the constants ϵ_0 and μ_0 combined to the vacuum speed of light $c_0 = 1/\sqrt{\epsilon_0\mu_0}$. This Master Equation represents an eigenvalue problem with $\mathbf{H}_{\mathbf{k}}$ as eigenmodes of the function (2.13) [2]. Any linear combination of eigenmodes is still a valid solution to the Master Equation. The operator $\hat{\Theta}$ acting on the eigenmodes is Hermitian and creates a complete set of orthonormal eigenfunctions with real eigenvalues [2].

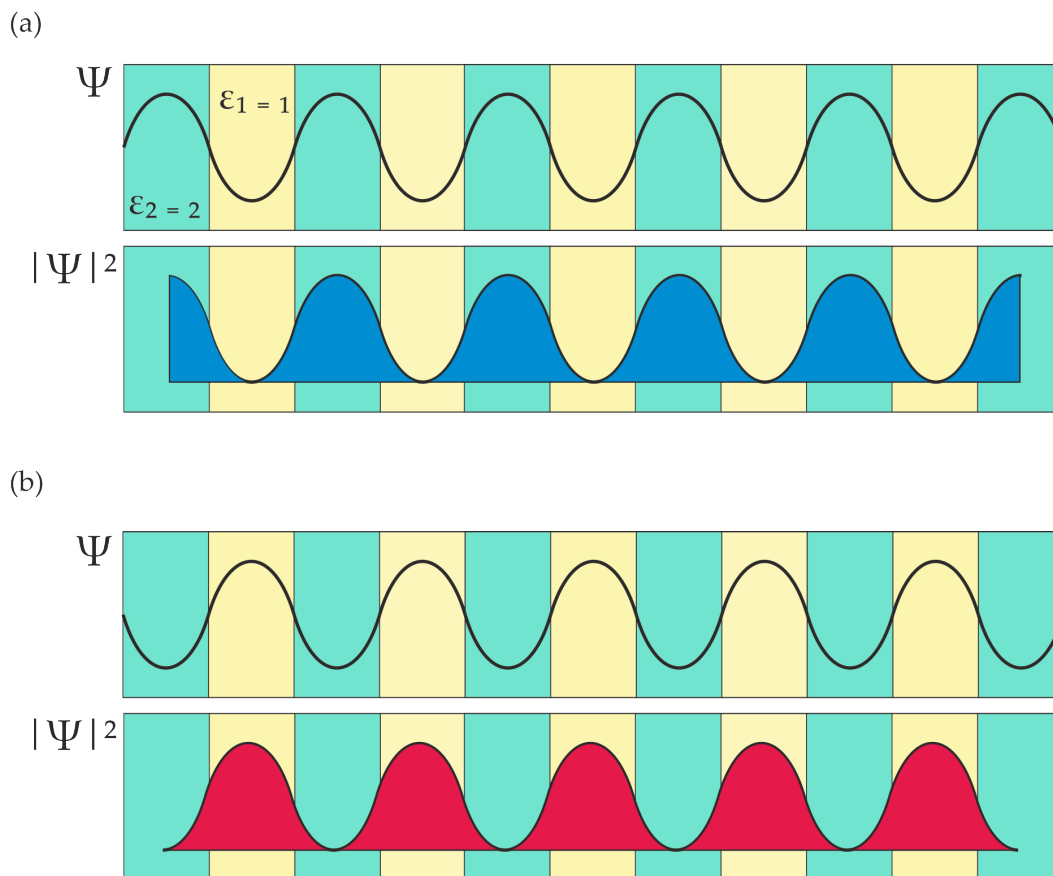


FIGURE 2.2: Schematics of a harmonic sequence of high and low refractive index regions with $\epsilon_2 = 2$ and $\epsilon_1 = 1$. The solution to a propagating wave in such a sequence is given by a Bloch mode. The examples of modes concentrating their energy in the high- refractive index regions (a) and the low-refractive index regions (b) are both valid solutions. Their different concentration of the energy leads to a differences in frequencies of these modes and a forbidden range of energies called the photonic band gap.

In order to find the lowest order eigenmodes of $\mathbf{H}(\mathbf{r})$, the functional

$$\left(\frac{\omega_{\mathbf{k}}}{c_0}\right)^2 \rightarrow \min_{\omega_{\mathbf{k}}} \frac{\int_{dr^3} |(\nabla + i\mathbf{k}) \times (\nabla + i\mathbf{k}) \times \mathbf{H}_{\mathbf{k}}|^2 d\Omega}{\int_{\Omega} \epsilon |\mathbf{H}_{\mathbf{k}}|^2 dr^3} \quad (2.14)$$

must be minimized by maximizing the denominator. This is achieved through an overlap of the high intensity of the electric fields with high dielectric constant areas [2]. Figure 2.2 depicts orthogonal solutions to the eigenmodes with their energies concentrated in either the high or low-dielectric-constant areas. Both solutions

are representing Bloch waves with the same periodicity as the periodic function of the refractive index and are valid solutions of (2.13). The modes concentrating their energy in the high-refractive index regions lead to large denominators and smaller frequencies. Modes experiencing low refractive index regions lead to small denominators and large frequencies. The differences in frequencies of the modes form a forbidden range of energies of the modes which is known as the photonic band gap.

Scale Invariance of the Master-Equation

The derived Master-Equation (2.13) for PhCs is scale invariant as there is no constant with the dimension of length in it [2]. This leads to a connection between electromagnetic eigenmode solutions which only differ in scale. Recalling the Master-Equation and defining a new dielectric function $\epsilon'(\mathbf{r})$ that is, for some scale parameter s , just a compressed or expanded version of the old one $\epsilon'(\mathbf{r}) = \epsilon(\mathbf{r}/s)$, a change of variables $\mathbf{r}' = s\mathbf{r}$ and $\nabla' = \nabla/s$ with $\epsilon(\mathbf{r}'/s)$ none other than $\epsilon'(\mathbf{r}')$ leads to

$$\nabla' \times \left(\frac{1}{\epsilon'(\mathbf{r}')} s \nabla' \times \mathbf{H}(\mathbf{r}'/s) \right) = \left(\frac{\omega}{cs} \right)^2 \mathbf{H}(\mathbf{r}'/s). \quad (2.15)$$

This is the Master-Equation again with eigenmode profile $\mathbf{H}'(\mathbf{r}')$ and frequency $\omega' = \omega/s$. The new profile and its corresponding frequency can be obtained by simply rescaling the old mode profiles and frequencies. This can be made use of to tailor the resonance wavelength of a given structure to a wanted value.

Photonic Crystal Cavities

If the periodicity of a one-dimensional PhC is broken up, a defect state in the material evolves and creates a localized field of high energy. The modes localized in the defect region are confined within a small, finite space and therefore quantized into discrete frequencies [2].

Changing the properties of the defect region generates different sets of quantized frequencies in the that region. This may either pull a mode down into the band gap from the upper bands which are referred to as the air bands from now on or push modes up into the gap from the lower bands

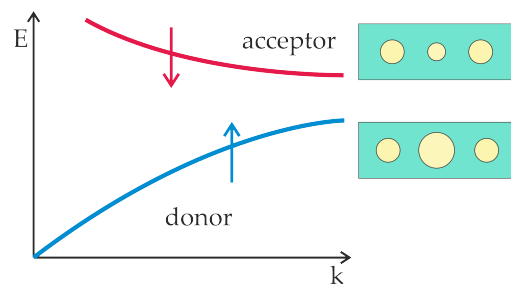


FIGURE 2.3: Schematics of the donor-acceptor model.

which are referred to as the dielectric band. By increasing the radius of a defect hole, modes are pulled into the band gap from the dielectric band and an acceptor defect state is created. By decreasing the radius of an individual hole modes from the air band are pulled into the band gap and a donor defect state is created as shown in figure 2.3 [6]. The best spatial localization of a defect mode is achieved when its frequency is near to the center of the band gap [6].

2.2 Atom-Light Interaction

For many physical considerations including only one atomic transition, e.g. the transition related to a resonant cavity mode, it is sufficient to consider an atom as a two-level system. By choosing a suitable basis, making use of the Rotating-Wave-Approximation and solving the Von-Neumann equation, the optical Bloch equations describing the states of two-level atoms will be derived in this chapter.

Two-Level Atom

A two-level atom has two energy levels, $|g\rangle$ and $|e\rangle$, separated by the energy $\hbar\omega_0$. The excited state $|e\rangle$ can be reached through optical excitation with the resonant frequency ω_0 [7]. In the two-level atom only transitions between the the ground and excited state at the decay rate Γ_0 can happen. In order to consider off-resonant excitation, the detuning Δ is introduced. The eigenvectors $|e\rangle$ and $|g\rangle$ span a two-dimensional Hilbert space. Therefore, the interaction of the atom with the electromagnetic field can be approximated as an electric-dipole interaction,

$$\hat{H}_A = E_g |g\rangle \langle g| + E_e |e\rangle \langle e|. \quad (2.16)$$

In the so-called dipole approximation, the wavelength of the electric field \mathbf{E} applied to the atom is considered to be much larger than the extent of the atom [8]. Therefore, the dipole moment of a two-level atom is approximated by

$$\hat{\mathbf{d}} = -e_0 \cdot \hat{\mathbf{x}} \quad (2.17)$$

where $\hat{\mathbf{d}}$ is the dipole operator, $\hat{\mathbf{x}}$ the position operator and $e_0 \approx 1.602 \cdot 10^{-19}$ C is the elementary charge. Assuming that the atom possesses inversion symmetry, i.e. that the energy eigenstates of the atom are either symmetric or anti-symmetric makes the terms $\langle e | \hat{\mathbf{x}} | e \rangle$ and $\langle g | \hat{\mathbf{x}} | g \rangle$ vanish. Then, one gets the following expectation value of the dipole operator

$$\langle \psi | \hat{\mathbf{d}} | \psi \rangle = -e_0 \left(\underbrace{|c_e|^2 \langle e | \hat{\mathbf{x}} | e \rangle}_{=0} + c_e c_g^* \langle g | \hat{\mathbf{x}} | e \rangle + c_g c_e^* \langle e | \hat{\mathbf{x}} | g \rangle + \underbrace{|c_g|^2 \langle g | \hat{\mathbf{x}} | g \rangle}_{=0} \right). \quad (2.18)$$

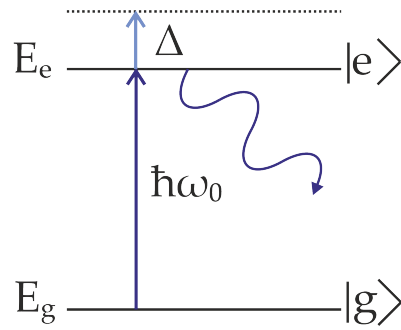


FIGURE 2.4: Schematic of a two-level atom with the ground and excited state $|g\rangle$ and $|e\rangle$ and the corresponding energies E_g and E_e . Δ depicts the detuning. The levels are separated by the energy $\hbar\omega_0$.

Density Matrix

To study the processes within atoms it is necessary to switch to a statistical description of atomic ensembles. Due to the Ergodic hypothesis an expectation value for a system of many atoms can be treated equally as an expectation value to the time-evolution of a single atom. The density matrix operator $\rho = |\psi\rangle\langle\psi|$ describes the behavior of a mixed quantum state with the wave function ψ [9]. For a two-level atom, the density matrix

$$\rho = (c_g |g\rangle + c_e |e\rangle) (c_g^* \langle g| + c_e^* \langle e|) = \begin{pmatrix} c_g c_g^* & c_g c_e^* \\ c_e c_g^* & c_e c_e^* \end{pmatrix} = \begin{pmatrix} \rho_{gg} & \rho_{ge} \\ \rho_{eg} & \rho_{ee} \end{pmatrix}. \quad (2.19)$$

includes the population for the ground and excited state in the diagonal elements and the coherences of the atoms in the off-diagonal elements. The expectation value of an operator A can be computed using the following relation

$$\langle A \rangle = Tr\{\rho A\}. \quad (2.20)$$

The advantage of the density operator lies in the fact that it can be applied to a statistical mixture of pure states [9]. If the atoms are in state $|e\rangle$ with probability p_e and in state $|g\rangle$ with probability p_g , the density operator $\rho = p_e |e\rangle\langle e| + p_g |g\rangle\langle g|$ can be defined and used to compute the average values of observables

$$\langle A \rangle = Tr\{\rho A\} = p_e \langle e| A |e\rangle + p_g \langle g| A |g\rangle. \quad (2.21)$$

The equation describing the time-evolution of the density matrix is given by the Von-Neumann equation

$$\frac{\partial \rho(t)}{\partial t} = -\frac{i}{\hbar} [\hat{H}(t), \rho(t)] \quad (2.22)$$

where $\hat{H}(t)$ describes the Hamiltonian of the system [8]. This equation does not consider any decoherence processes, e.g. spontaneous emission or collision. These effects can be included into the calculation by adding the Lindblad operator which sums over all dissipative channels m which an atom can emit to [8],

$$\hat{L}_D(\rho) = -\frac{1}{2} \sum_m (C_m C_m^\dagger \rho + \rho C_m^\dagger C_m) + \sum_m C_m \rho C_m^\dagger. \quad (2.23)$$

A two-level atom only allows a transition between the ground and excited state with the decay rate Γ_0 $C_1 = \sqrt{\Gamma_0} |g\rangle\langle e|$. Therefore, the Lindblad operator (2.23) for a two-level atom can be simplified to [8]

$$\hat{L}_D(\rho) = \Gamma_0 \begin{pmatrix} \rho_{ee} & -\rho_{ge}/2 \\ -\rho_{eg}/2 & -\rho_{ee} \end{pmatrix}. \quad (2.24)$$

Rotating-Wave Approximation

The atom-light interaction is given by the atom-field Hamiltonian

$$\hat{H}_{\text{A-F}} = -\mathbf{d} \cdot \mathbf{E}(t, \mathbf{x}). \quad (2.25)$$

where $\mathbf{E}(t, \mathbf{x})$ describes a classical, monochromatic plane wave

$$\mathbf{E}(t, \mathbf{x}) = \frac{1}{2} (\mathbf{E}_0 \cdot e^{i\omega t} + \mathbf{E}_0^* \cdot e^{-i\omega t}). \quad (2.26)$$

The total Hamiltonian of the system is given by the sum of the atom's Hamiltonian (2.16) and the atom-field Hamiltonian (2.16)

$$\hat{H}(t) = \hat{H}_A + \hat{H}_{\text{A-F}}^{\text{RWA}}. \quad (2.27)$$

For a strong interaction of the plane wave (2.26) with the atom, its frequency has to be close to the atomic transition frequency $\omega \approx \omega_0$. A unitary transformation matrix,

$$\begin{pmatrix} 1 & 0 \\ 0 & e^{i\omega t} \end{pmatrix}, \quad (2.28)$$

is used to switch into a dynamics of the atom which oscillates with the same frequency ω as the light [8]. The transformed density matrix is then given by

$$\tilde{\rho} = U^\dagger \rho U = \begin{pmatrix} \rho_{\text{gg}} & \rho_{\text{ge}} e^{i\omega t} \\ \rho_{\text{eg}} e^{-i\omega t} & \rho_{\text{ee}} \end{pmatrix}. \quad (2.29)$$

Inserting equation (2.29) into the Von-Neumann equation (2.22) leads to the transformation of the Hamiltonian,

$$\tilde{H} = U^\dagger H U - i\hbar U \frac{\partial U}{\partial t}, \quad (2.30)$$

which can be calculated by inserting the transformed density matrix (2.29) into (2.30) and simplified by the dipole matrix elements $\mathbf{d}_{\text{eg}} = \langle e | \hat{\mathbf{d}} | g \rangle$

$$\tilde{H} = \begin{pmatrix} 0 & \frac{\mathbf{d}_{\text{eg}}}{2} (E_0 + E_0^* e^{i2\omega t}) \\ \frac{\mathbf{d}_{\text{eg}}}{2} (E_0 e^{-i2\omega t} + E_0^*) & \hbar(\omega_0 - \omega) \end{pmatrix}. \quad (2.31)$$

where the energy of the ground state is set to zero [8].

The off-diagonal elements of the Hamiltonian (2.31) contain terms oscillating at twice the optical frequency. These terms can be neglected as these oscillations are

much faster than the evolution timescales of the atomic system [8]. This step is known as the rotating wave approximation [8] and simplify the Hamiltonian to

$$\tilde{H} = \hbar \begin{pmatrix} 0 & \Omega_0/2 \\ \Omega_0^*/2 & -\Delta \end{pmatrix} \quad (2.32)$$

where the detuning is $\Delta = \omega - \omega_0$ and the Rabi frequency is defined as

$$\Omega_r = \frac{\mathbf{d}_{eg} \cdot \mathbf{E}_0}{\hbar}. \quad (2.33)$$

Bloch Equations

The transformation of the Lindblad operator (2.23) into the rotating frame is simply given by $\tilde{L}(\tilde{\rho}) = L(\rho)$ [8]. Adding the Lindblad Operator (2.23) to the Neumann equation (2.22) results in the Lindblad master equation

$$\frac{\partial \rho(t)}{\partial t} = -\frac{i}{\hbar} [\hat{H}(t), \rho(t)] + \hat{L}_D(\rho). \quad (2.34)$$

Writing down each component of the time-evolution of $\rho(t)$ leads to the optical Bloch equations:

$$\frac{\partial}{\partial t} \rho_{gg} = \Gamma_0 \rho_{ee} + \frac{i}{2} \Omega_r (\rho_{ge} - \rho_{eg}) \quad (2.35)$$

$$\frac{\partial}{\partial t} \rho_{ge} = -\left(\frac{1}{2}\Gamma_0 + i\Delta\right) \rho_{ge} + \frac{i}{2} \Omega_r (\rho_{gg} - \rho_{ee}) \quad (2.36)$$

$$\frac{\partial}{\partial t} \rho_{eg} = -\left(\frac{1}{2}\Gamma_0 - i\Delta\right) \rho_{eg} + \frac{i}{2} \Omega_r (\rho_{ee} - \rho_{gg}) \quad (2.37)$$

$$\frac{\partial}{\partial t} \rho_{ee} = -\Gamma_0 \rho_{ee} + \frac{i}{2} \Omega_r (\rho_{eg} - \rho_{ge}) \quad (2.38)$$

These equations describe the interaction of the oscillating electric field with the atom. The components ρ_{gg} and ρ_{ee} describe the probabilities of finding an atom in its ground or excited state respectively. Numerically, these equations can be solved using the Runge-Kutta method which is discussed in the next chapter, *Basics of the Simulation*.

Rabi Oscillations

In the last sections, applying a monochromatic, resonant, electromagnetic field lead to a time evolution of the density matrix given by the optical Bloch equations. The solutions to these equations show the oscillations of the probabilities of finding an

atom in its excited or ground state and are called the Rabi oscillations. Due to collisions of the atoms, spontaneous emission and other effects which are balancing the probabilities of finding an atom in a certain state, a Rabi oscillation is damped and stops after a certain time. Then, an equilibrium of finding the atom in its excited or ground state the atom is achieved.

2.3 Cavity Quantum Electrodynamics

This chapter gives an overview of the interaction of two-level atoms with confined modes in PhC cavities. In order to characterize the interaction strength, cavity quantum electrodynamics parameters as the quality factor, the mode volume, the coupling strength and the cooperativity are introduced.

Quality Factor

The quality factor is a dimensionless parameter which characterizes a resonator's full width half maximum $\Delta\omega$ relative to its resonance frequency ω_r [10],

$$Q = \frac{\omega_r}{\Delta\omega}. \quad (2.39)$$

It can be derived by looking at the decay of the time-dependent electric field confined in the cavity. The time domain signal of the resonant electric field is described by

$$E(t) = e^{-t(\kappa - i\omega_r)} \cdot u(t), \quad (2.40)$$

where κ is the cavity decay rate and $u(t)$ is the electric field envelope. Looking at the spectral energy density

$$|E(\omega)|^2 = \frac{1}{\kappa^2 + (\omega - \omega_r)^2}, \quad (2.41)$$

to determine the half-maximum frequencies at $\omega = \omega_r \pm \kappa$ leads to the full width half maximum $\Delta\omega = 2\kappa$. This can be substituted into expression (2.39) leading to

$$Q = \frac{\omega_r}{2\kappa}, \quad (2.42)$$

as well as to the definition of the cavity decay rate

$$\kappa = \frac{\omega_r}{2Q} = \frac{\pi \cdot c}{\lambda_{\text{res}} Q} \quad (2.43)$$

where c is the vacuum speed of light and λ_{res} the resonance wavelength. The larger the quality factor of a cavity is, the smaller the decay rate of the field would be and the longer is the photon lifetime in the cavity [7].

Mode Volume

The mode volume V_m gives a measure of the spatial confinement of the electromagnetic field in a cavity [11]. It is given by

$$V_m = \frac{\int_V \epsilon(\mathbf{r}) |\mathbf{E}(\mathbf{r})|^2 d^3\mathbf{r}}{|\mathbf{E}_{\max}(\mathbf{r})|^2} \quad (2.44)$$

where $\epsilon(\mathbf{r})$ is the relative permittivity, \mathbf{r} the position vector and $\mathbf{E}_{\max}(\mathbf{r})$ the maximum of the electric field. The integral represents an integration over the whole space. The smaller the mode volume is, the smaller the space in which a photon is squeezed and the stronger the interaction between a single atom within the mode volume of the photon can be.

Vacuum Rabi frequency

The strength of an atom-photon interaction can be described by the vacuum Rabi frequency g which is derived from the field quantization. It is a feature of the mode itself and is given by

$$g = 2 \cdot \frac{1}{\hbar} \sqrt{\frac{\hbar\omega_0}{2\epsilon_0 V_m}} \mathbf{E}(\mathbf{r}_a) \cdot d_{ge} \quad (2.45)$$

where \mathbf{r}_a depicts the atom position. The vacuum Rabi frequency is used in the calculation of the cooperativity.

Purcell Factor

The decay rate of an atom is not an intrinsic property and is strongly dependent on its surroundings. The Purcell factor F_p is a number which describes the modification of an atom's decay rate in an environment different from vacuum. An emitter in an optical cavity emits photons at a decay rate $\Gamma_{\text{cav}} = F_p \cdot \Gamma_0$.

For a single mode, the Purcell factor can be calculated using

$$F_p = \frac{3}{4\pi^2} \left(\frac{\lambda}{n} \right) \left(\frac{Q}{V} \right). \quad (2.46)$$

where λ is the free space wavelength and n is the refractive index of the material. For multiple modes of a resonator, a numerical calculation of the Purcell factor is necessary which will be discussed in the chapter *Basics of the Simulation*.

Cooperativity

The cooperativity is a dimensionless parameter measuring the ratio of the coherent to incoherent phenomena in a cQED system. Thereby, it weighs the square of the wanted atom-cavity coupling rate g against the unwanted loss mechanisms κ and $\Gamma_{0\perp}$

$$C = \frac{g(\mathbf{r}_a)^2}{2\kappa \cdot \Gamma_{0\perp}} = \frac{3\lambda_{\text{res}}^3 |\mathbf{E}(\mathbf{r}_a)/\mathbf{E}_{\text{max}}|^2 Q}{8\pi^2 V_m}. \quad (2.47)$$

The parameter κ shows the photon decay rate from the cavity and $\Gamma_{0\perp}$ is the decay rate of the atom into all other modes except the desired cavity mode. Note, that the total decay rate of the atom Γ_0 is given by the sum of all decay rates

$$\Gamma_0 = \Gamma_{0\perp} + \Gamma_{\text{cav}} \quad (2.48)$$

where $\Gamma_{0\perp}$ only includes the decay rate into dissipative channels and Γ_{cav} the one into a cavity mode.

Physically, the cooperativity can be interpreted as a scaled number of absorption and emission cycles between a confined photon and the atom before the photon in the resonator is lost. As the cooperativity is proportional to Q/V_m , high cooperativities can be achieved through small mode volumes and large quality factors.

3 Basics of the Simulation

This chapter aims at introducing the finite difference time domain (FDTD) method and the Lumerical software to the reader. Moreover Matlab codes, including a Range-Kutta code for solving the optical Bloch equations and a code setting up a trajectory of an atom moving through a PhC are presented.

3.1 Lumerical

3.1.1 The FDTD Method

FDTD solutions is a fully vectorial, time-domain solver of Maxwell's Equations. The electric and magnetic fields for future time steps are calculated based on the fields at former time steps. There is an offset of the H field by a half-time and a half-position step compared to the E field is made [13].

$$\begin{aligned} \mathbf{E}(x, t) &= \mathbf{E}^{q,n}, \\ \mathbf{H}(x, t) &= \mathbf{H}^{q+1/2,n+1/2}, \end{aligned}$$

Then, the derivatives in Maxwell's curl equations are approximated as *finite differences* or slopes for discretized time steps n and position steps q . In order to compute the vector components of the electric and magnetic fields at each time step, they are sampled on a Yee cell which can be seen in figure 3.1. A Yee cell represents a part of a spatial and temporal grid. Each field component is solved at a slightly different location within the grid cell, as shown in figure 3.1. The electric and magnetic field at later times are updated based on the fields at previous time steps based on the following equations,

$$\begin{aligned} \mathbf{E}^{n+1} &= \mathbf{E}^n + \alpha \nabla \times \mathbf{H}^{n+1/2}, \\ \mathbf{H}^{n+3/2} &= \mathbf{H}^{n+1/2} + \beta \nabla \times \mathbf{E}^{n+1}, \end{aligned}$$

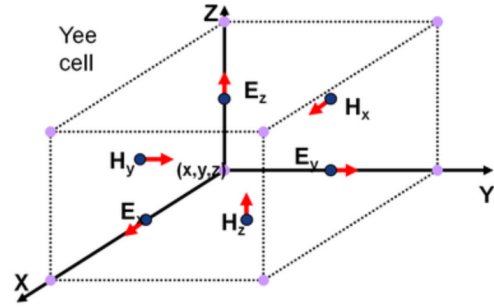


FIGURE 3.1: A Yee Cell represents a part of a spatial and temporal grid at which the field components are solved [12]

where the parameters α and β represent simulation-dependent constants [13]. The data collected from the FDTD solver is interpolated to the origin of the Yee cell so that the end user receives a discretized map of points at which the fields are solved for their analysis. [12]. The size of the Yee cell depends on the mesh size of the simulation.

The FDTD method leads to results with high accuracy in the time and spatial domain as only few initial approximations must be made by setting the offset of the H field by one half time step compared to the E field in the beginning [13]. Moreover, the method is used in simulations where geometric optics breaks down and where devices on the order of the size of the wavelength have to be simulated [13].

The main benefit of FDTD is that it allows one to handle almost any kind of structure with a precise mesh as the fields are computed at all discretized spatial points within the simulation domain at every time step. This makes it possible to observe the electric fields as a movie through time. Using the Fourier transform of the electric field function, it becomes also possible to investigate the resonance frequencies of the field which is especially useful for studying optical resonators.

3.1.2 Simulation Tools and Objects

In order to run simulations with the FDTD method the software *Lumerical* is used. Lumerical offers a graphical user interface where it is possible to add a simulation region, components, sources and monitors to a simulation. These features extracted out of the *main tool bar* as depicted in figure 3.2 are described in the following sections.

Simulation Region

Every simulation allows only one *simulation region* where the *time of the simulation*, the *background refractive index*, the *simulation volume geometry*, the *mesh settings* and *boundary conditions* can be selected appropriately [14]. *PML*, i.e. perfectly matched layer, boundary conditions are absorbing boundary conditions suppressing any reflection from the boundary of the simulation region. They can be used to extend structures through the boundaries to mimic an infinitely large structure. *Metal* boundary conditions are used as perfectly reflecting boundaries. *Periodic* boundaries are employed to simulate infinitely periodic structure. *Bloch* boundaries are similar to the periodic ones but are used when a phase shift of the fields exists between unit cell boundaries. *Symmetric* and *anti-symmetric* boundary conditions are useful where a structure and source have symmetry. They reduce the simulation volume and time. The result of a half, quarter or eighth of the simulation is unfolded

across the planes of symmetry to get the simulation result of the whole region [14].

Structures and Objects

The structures and objects that can be added from the *structures* menu in the main toolbar contain predefined structures e.g. *circles* and *rectangles*. They can be combined in *structure groups* where the properties of all objects within a group can be set simultaneously using a *setup script*. It is possible to import images of an atomic-force microscope for presenting the geometries of an already fabricated structure [14].

Sources

Various sources can be added from the source menu in the main tool bar. A *dipole point source* represents an oscillating point source and can be used to simulate an atom. Moreover, *Gaussian*, *plane wave sources* or *total-field-scattered-field plane waves* can be added [14].

Monitors

Monitors allow to collect data from the simulation. The *refractive index monitor* is used to record the refractive index as a function of position. The *field time monitor* is capturing the data of the electric and magnetic fields as a function of time. A *movie* is saving a file showing the time-evolution of the fields. The *frequency-domain field profile monitor* or *power monitors* are collecting the data of the fields of the transmission, reflection, absorption for different frequency points. These monitors return the field profiles and are useful for analyzing the fractions of power transmitted through a surface [14].

Analysis Groups

Complex analysis with data from any monitors can be done in an *analysis group*. The data of any object can be collected by a C++ based script in the analysis group and used in post-processing calculations. The results from an analysis group can be viewed and collected the same way as monitor results [14].

Optimization and Parameter Sweep

Next to the script editor, *optimizations and parameter sweeps* can be added to a simulation. In the edit window, it is possible to set which parameter(s) are varied or optimized and from which maximum to which minimum value the parameter is

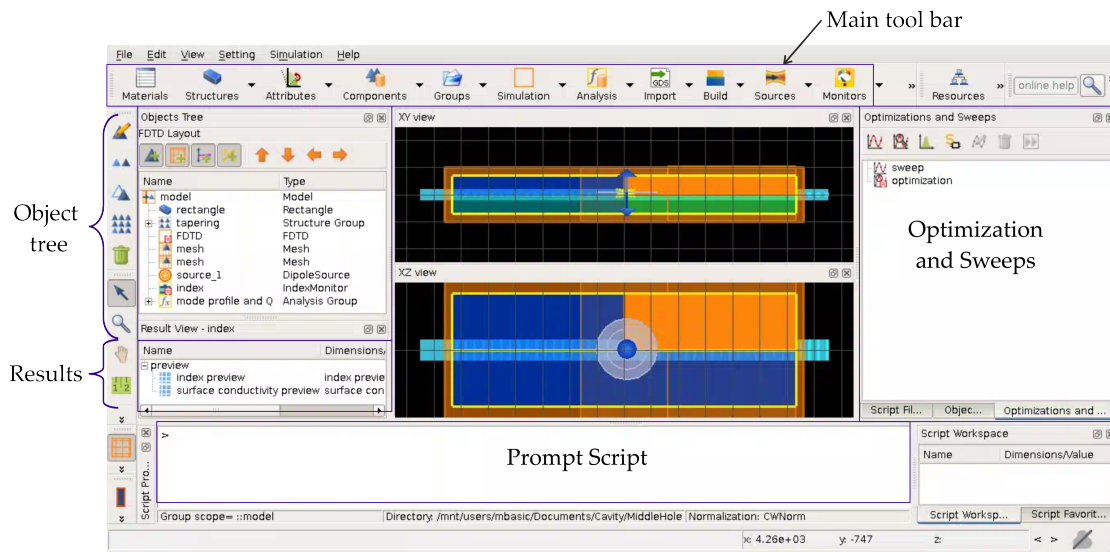


FIGURE 3.2: User interface of FDTD solutions. In the the *main toolbar* it is possible to add a simulation region, components, sources and monitors to a simulation. The *object tree* lists all components that are in a simulation. The *results* window lists all corresponding results. In the *Optimization and Sweeps* window, an Optimization or sweep can be started. The prompt script executes commands in Lumerical scripting language.

varied. For each varied parameter a separate simulation file is saved in a mutual folder. An optimization creates an additional figure of merit to track the trends of a parameter change [14].

Script environment

The *script environment* includes the script file editor and the script prompt. The script prompt executes only one command at a time and the editor allows to collect groups of commands, save them as a script file or to load and run them again. It is possible, just like in the graphic editor, to add objects and set their properties, collect results, manipulate and plot data, to print results to the script prompt and to export data to different formats [14].

Time to Simulate and Memory Requirements

A simulation can be run in 2D or 3D. A 3D simulation requires a memory proportional to $\propto V \cdot (\lambda/dx)^3$ and a simulation time $\propto V \cdot (\lambda/dx)^4$ with V depicting the simulation volume, λ the propagating wavelength and dx the mesh size in each direction. In the 2D case, a memory of $\propto V \cdot (\lambda/dx)^2$ and a simulation time $\propto V \cdot (\lambda/dx)^3$ are required. The finer the mesh, the more Yee cells where the fields

must be calculated. Therefore, it is always recommended to do initial simulations with relatively coarse mesh or in 2D instead of 3D to save a lot of time in the long run [14].

3.1.3 A Photonic Crystal Cavity Simulation

The following section describes the set up of a PhC cavity simulation of and how to analyze different characteristics, e.g. the quality factor and the field profiles, the band structure of the crystal and the Purcell factor of a dipole source.

Band structure

As the PhC is periodic, it is only necessary to simulate one unit cell of the structure for the band structure calculation [15]. The variables used in this simulation including the periodicity, the apodization parameters, and the vector \mathbf{k} are set in the 'model' analysis group setup script.

The previously described Bloch boundary conditions are used at each boundary of the unit cell. Then a parameter sweep is started varying the \mathbf{k} -vectors. Each produced file of the parameter sweep, one simulation for each \mathbf{k} , gives the simulation results of the band frequencies for a particular \mathbf{k} -vector.

As the goal of the band structure simulation is to see whether the structure supports the band gap for all polarizations, sources capable of exciting all modes of interest for the device are created. A number of randomly oriented and randomly distributed dipole sources is used. It is also possible to set the dipole orientations to only excite certain modes in order to isolate bands of interest [15]. Symmetric boundary conditions can also be used in order to restrict the possible modes and to isolate the bands [15].

The bandstructure analysis group loads the time signals from each time monitor for each field component and apodizes the signals in order to filter out the beginning and end portions of the time signal to remove any transit time behavior [15]. The Fourier transforms of the apodized time signals is then used to calculate the peaks at the resonance frequencies for each \mathbf{k} -vector. Several Fourier transforms of each time monitor are summed to ensure that all the resonant frequencies of a mode are found just in case a time monitor is located in a high-symmetry point [15].

To sum it up, the band structure calculation sets certain values of \mathbf{k} vectors and then analyses the spectra. The frequencies of the peaks of the spectra for each \mathbf{k} vector are plotted against \mathbf{k} , resulting in the band structure.

Quality Factor and Field Profiles

To begin with the set up of the simulation of the quality factor and the field profiles, a simulation region having a simulation time of 3000 fs, a background refractive index of $n = 1$, a simulation volume geometry of $x = 12000$ nm, $y = 1400$ nm and $z = 1300$ nm and stabilized PML boundary conditions is set up. In this specific case, the PhC cavity is created out of etched holes in a silicon nitride slab. Therefore a rectangle with the approximate refractive index of silicon nitride $n = 2$ for a wavelength of 780 nm is added to the simulation region. The rectangle is included into the simulation before the circles/ holes as depicted in figure 3.3 as the added objects are written into the simulation in the order of the object tree.

The rectangle or slab expands through the PML layers at both sides of the simulation boundaries in order to avoid artificial reflections as can be seen in figure 3.3 from the blue slab expanding through the orange simulation boundaries. For the purposes of this analysis, the PhC cavity is assumed to have 14 holes at each side of the mirror region and seven holes in the tapered region.

The mesh in the x -, y - and z - direction is set by adding a mesh override region with the mesh steps $dx = dy = dz = 7$ nm. Setting a small mesh size increases the calculation time but also the resolution of the holes and therefore the accuracy of the result [16].

For the initial phase of a design, the approach is to start with coarse meshes to obtain initial results and to move to finer meshes to obtain the final data of a simulation [16].

A dipole source injects a pulsed signal into the PhC cavity. As it is assumed that the modes of the cavity represent TE modes, the polarization of the dipole source is set to be TE, i.e. parallel to the y axis. In order to adapt the dipole's radiation to the characteristics of a Rubidium atom, the center wavelength of the dipole is set to 780 nm referring to the wavelength of the D_2 transition. The intensity of the injected light pulse from the dipole has to be excluded out of the final field profiles otherwise the fields depict a spot of high intensity at the dipole position.

As the cavity is confining the fields much longer compared to the initial length of the dipole pulse, the effects of the source can be cut out by using a time window

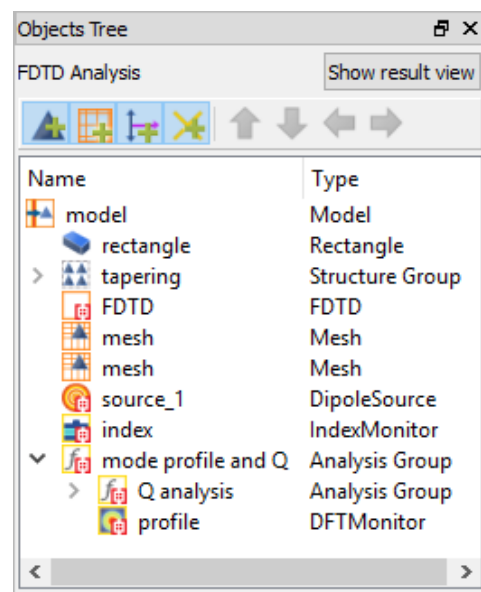


FIGURE 3.3: Object tree setting up the simulation for a PhC cavity analysis.

for processing the electric field envelope. The electric field of the dipole pulse is intentionally not included in this window function and only the time intervals of the field where the frequencies of the cavity modes are remaining are analyzed and then interpolated to determine the complete time signal of the electric field.

Four time monitors spread over a region of the cavity's defect region are chosen to capture the behavior of the electric and magnetic fields. To capture the modal fields, the frequency domain profile monitors are used. These monitors are stored in an analysis group called *mode profiles*.

As the structure exhibits three planes of symmetry, symmetric and anti-symmetric boundary conditions are used to reduce computation time. However, the cost of symmetry boundary conditions is that they forbid certain modes from appearing in the results, i.e. the modes that do not exhibit the same symmetry relation as the boundary condition. For this PhC cavity, there is a plane of symmetry through the center of the slab ($x = 0$ plane). Using a symmetric boundary condition on this plane will only allow TE modes and eliminate TM modes from the results. Since for this structure the cavity modes are expected to be TE, the symmetric boundaries represent the right conditions here [16]. The other planes ($y = 0$ plane and $z = 0$ plane) are supposed to be anti-symmetric. Note, it is important to set the dipole away from the symmetric and anti-symmetric boundaries or a highly symmetric point to ensure that is coupling to all the allowed modes.

When studying resonators, the auto-shutoff feature of FDTD Solutions must be disabled. The auto-shutoff is a measure of the energy left in the simulation region. If this value is small enough, a simulation is stopped before the end of the simulation time. An optical resonator only traps a small fraction of the original excitation energy injected in the simulation. As a result the auto-shutoff can assume that the energy left in the simulation is too small to continue the simulation and trigger an early termination of the simulation. To fully capture the complete dynamics of the cavity however, the autoshutoff can be disabled by unchecking the "use early shutoff" in the Advanced Options tab of the FDTD simulation region [16]. Finally, the analysis group can determine the Q-factor the same way as described in the *Cavity Quantum Electrodynamics* chapter and obtains the data of the electric mode profile.

Purcell Factor

The Purcell factor is describing the spontaneous emission rate modification of an emitter inside a cavity or resonator [17]. Since the emission rate of the dipole in the simulation is proportional to the local density of optical states in our study, the Purcell factor is given by the power emitted by a dipole source in the environment

of the resonator by the power emitted by the dipole in free space. Therefore, all the symmetric and anti-symmetric boundary conditions must be disabled as those are acting as a mirror for the single dipole source and increasing the Purcell factor artificially. Then, the simulation must run until the fields have completely decayed to really receive the whole power emitted by the dipole source in the environment [17].

Common Simulation Problems

Typically, PML boundary conditions which absorb most incident radiation propagating away from the cavity are used. It is important to leave enough distance between the cavity and the PML boundaries. If the boundaries are too close to the cavity, they absorb the non-propagating local evanescent fields which exist within the cavity. A rule of thumb is to leave at least half a wavelength of distance between the boundaries and the structure in the y and z direction [18].

In the x direction, the silicon nitride slab must be extended through the simulation boundaries to mimic an infinite slab. If an interface between the slab and the PML in the x -direction is included, this can cause artificial confinement caused by the reflection on the interface. Using the “extend through PML” option in the FDTD region settings avoids this artificial confinement [18]. Moreover, stabilized PML boundary conditions adapt the amount of PML layers at the boundaries and maintain the simulation stability.

To get valid Q-factor results, it is important to include an integer number of mesh cells per lattice constant in the mirror regions. This makes sure that the holes are all meshed in the same way. Otherwise, each hole has a slightly different size and shape in the simulation and the periodicity is not distinguished. Moreover, it is important to make sure that enough PhC periods are included in the mirror regions. Using a low number of unit cells can result in a poor confinement of the electromagnetic fields in the transverse direction [18].

3.2 Matlab

3.2.1 Runge-Kutta Method

In the *Atom-Light Interaction* chapter the optical Bloch equations describing the interaction of the oscillating electric field with an atom were derived. Numerically, these equations can be solved using the Runge-Kutta method. This method is used to approximate the solution of first order differential equations given by

$$\frac{dy(t)}{dt} = y'(t) = f(y(t), t) \quad (3.1)$$

with some known initial condition $y(t_0) = y_0$ [19]. The math behind this method is simple to understand by starting from a first-order Euler approximation. The derivative of (3.1) at the time t_0 is then given by

$$y'(t_0) = f(y(t_0), t_0)$$

Expanding $y(t)$ around t_0 and assuming a time step h leads to

$$y(t_0 + h) = y(t_0) + y'(t_0)h + y''(t_0)\frac{h}{2} + \dots$$

Dropping all the orders higher than the linear term yields to [19]

$$y(t_0 + h) \approx y(t_0) + y'(t_0)h = y(t_0) + k_1h.$$

This algorithm already provides one possibility to solve the differential equation (3.1) numerically. However, it is necessary to use relatively small time steps to get accurate results. The fourth order Runge-Kutta produces more reasonable results in fewer steps by approximating the derivative after stepping half way through the time step h . Each of the slope estimates k_1 , k_2 , k_3 and k_4 from the fourth order Runge-Kutta can be described in the following way

$$\begin{aligned} k_1 &= f(y(t_0), t_0), \\ k_2 &= f\left(y(t_0) + k_1\frac{h}{2}, t_0 + \frac{h}{2}\right), \\ k_3 &= f\left(y(t_0) + k_2\frac{h}{2}, t_0 + \frac{h}{2}\right), \\ k_4 &= f(y(t_0) + k_3h, t_0 + h). \end{aligned}$$

The estimate k_1 is the slope at the beginning of the time step. This slope k_1 is used to step halfway through the time step. Then k_2 is an estimate of the slope at

the midpoint of the time step h which gives a better approximation to the slope. If the more accurate slope k_2 is used to step halfway through the time step h , then k_3 gives another improved estimate of the slope at the midpoint. Finally, the slope k_3 is used to step all the way across the time step to $t_0 + h$, and k_4 is an estimate of the slope at the endpoint [19].

Then, a weighted sum of these slopes is used to get the final estimate of $y(t_0 + h)$

$$y(t_0 + h) = y(t_0) + \frac{k_1 + 2k_2 + 2k_3 + k_4}{6}h \quad (3.2)$$

Note, this simulation method depends on the size step h . Larger values of h result in poorer approximations [19].

3.2.2 Monte-Carlo Analysis

The Monte-Carlo simulation used to simulate the trajectories and the states of atoms moving through the PhC cavity and to generate random trajectories of a complex system of many atoms. The speed distribution of the atoms follows directly from the Boltzmann distribution.

It is assumed that the probability of finding one atom with kinetic energy E decreases exponentially with the energy. This can be expressed mathematically via the Boltzmann distribution

$$f(E) = A \cdot e^{-E/k_B T}. \quad (3.3)$$

The Boltzmann distribution is taken to be a postulate and used to show how the Maxwell-speed distribution follows from it. If the energy in the Boltzmann distribution is just one-dimensional kinetic energy, then the expression becomes

$$f(v_z) = A \cdot e^{-\frac{mv_z^2}{2}} \cdot \frac{1}{k_B T} \quad (3.4)$$

This function must be normalized via the constant A . This is accomplished by integrating the probability from minus to plus infinity and setting it equal to one. Making use of the definite integral form

$$\int_{-\infty}^{\infty} e^{-x^2} dx = \sqrt{\pi}, \text{ with the substitution } x = \sqrt{\frac{m}{2k_B T}} v_z \quad (3.5)$$

allows one to normalize the function (3.4) via

$$A \cdot \sqrt{\frac{2k_B T}{m}} \int_{-\infty}^{\infty} e^{-\frac{m}{2k_B T} v_z^2} = 1 \text{ which gives } A = \sqrt{\frac{m}{2\pi k_B T}}. \quad (3.6)$$

Converting this relationship to one which expresses the probability in terms of speed in three dimensions gives the Maxwell speed distribution:

$$f(v) = 4\pi \left(\frac{m}{2\pi k_b T} \right)^{3/2} v^2 \cdot e^{-\frac{mv^2}{2k_b T}} \quad (3.7)$$

Comparing this expression to the normal distribution

$$f(x, \mu, \sigma) = \frac{1}{\sqrt{\pi\sigma^2}} e^{-\frac{(x-\mu)^2}{2\sigma^2}}, \quad (3.8)$$

with the expectation value μ and the standard deviation σ , it becomes clear that the standard deviation of the speed distribution (3.7) is given by $\sigma = \sqrt{\frac{k_b T}{m}}$.

The atoms in the Monte-Carlo code are initialized randomly with a velocity within $(-\infty, +\infty)$ and a probability given by the Maxwell distribution. However, the focus of this thesis will lie on analyzing one simple trajectory with the velocity $\mathbf{v} = \sigma \cdot \mathbf{v}_z = \sigma(0, 0, 1)$ to visualize the physical effects of an atom moving straight through the maximum field intensity of the centered hole in the PhC cavity. In the results reported in this thesis, the number of atoms is set to one and the intensity profile derived from FDTD is included into the simulation. Moreover, a map of position-dependent Rabi frequencies is included. The refractive index info of the slab is extracted from a 2D refractive index monitor from FDTD and expanded to 3D by reshaping the index region. The simulation region of the Matlab code finishes at the same boundaries as the FDTD simulation region. It is divided up into sections above, below, in front of and behind the slab as well as a section containing the holes within the slab to define the reflections at these boundaries if necessary.

A first loop updates the position and velocity vectors for each time step while another loop updates the components of the density matrix with the fourth-order Runge-Kutta method. The time steps at which the atom is observed need to be small enough for the Runge-Kutta code to approximate the derivatives of the optical Bloch equations properly.

4 Results

This chapter presents the final design of a one-dimensional PhC cavity beginning with the band structure and Bloch modes in the mirror region heading to the mode profile in the tapered region. Employing the previously described Matlab code, the interaction of a Rubidium atom with the confined light in the cavity is investigated. Finally, the thermal behavior of the cavity is analyzed.

4.1 Bandstructure

In the *Photonic Crystals* chapter, it has been described how certain wavelengths or frequencies of light are not allowed to pass a PhC which is leading to a forbidden range of energies forming a photonic band gap. As discussed, breaking the periodicity of a PhC creates a defect center in the structure supporting a localized photonic mode within the photonic bandgap. Choosing this mode in the defect region to match with a transition in an atom leads to atom-light interaction in the vicinity of PhC cavities. Therefore, the band gap in the mirror region has to support the transition frequency or wavelength of the atom, in this case the rubidium atom. The investigated transition in the atom corresponds to the D_2 line with a resonance wavelength λ_{D_2} and frequency f_{D_2} [20],

$$\lambda_{D_2} = 780.24 \text{ nm}, f_{D_2} = 384.23 \text{ THz}.$$

With the unit cell of the PhC cavity studied in this thesis a band gap supporting these values is achieved. The unit cell of the crystal consists of silicon nitride (Si_3N_4) with an air hole in the center of the unit cell which has the following properties,

$$\begin{aligned} \text{Periodicity } a &= 325 \text{ nm}, \\ \text{Radius } r &= 91 \text{ nm}, \\ \text{Width } w &= 426 \text{ nm}, \\ \text{Height } h &= 241 \text{ nm}. \end{aligned}$$

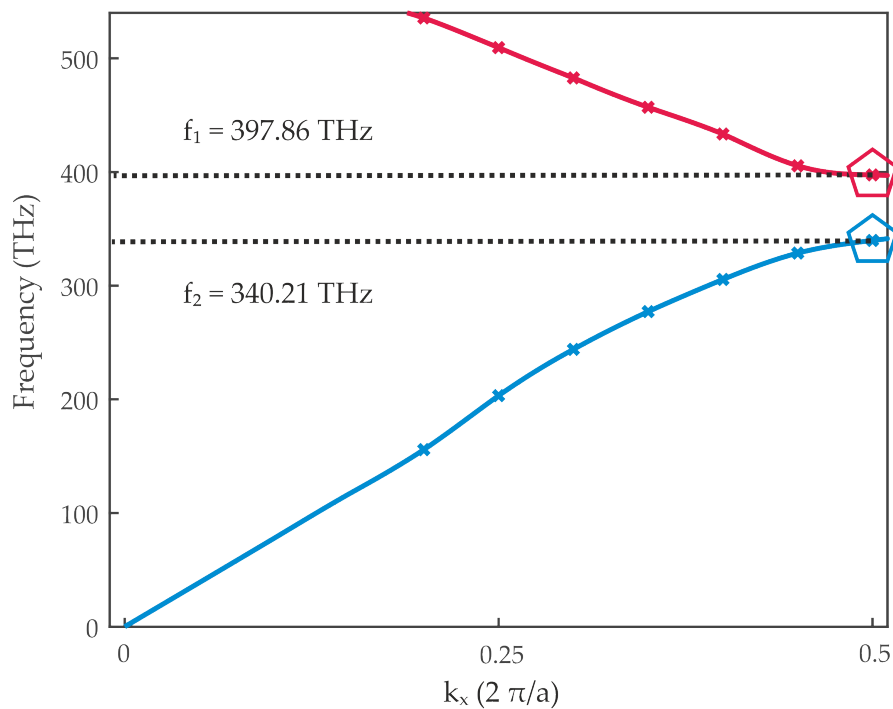


FIGURE 4.1: Simulated Band structure of the PhC mirror region. The band diagram exhibits a band gap from $f_1 = 340.21$ THz to $f_2 = 397.86$ THz. The polygons mark the frequency points used in the next section to calculate the Boch Modes. The crosses mark the frequency points extracted out of the band structure calculation.

The band diagram exhibits a band gap from $f_1 = 340.21$ THz to $f_2 = 397.86$ THz. This can be seen in figure 4.1. The aimed frequency of 384.23 THz corresponding to the D_2 Rubidium transition lies within this band gap. Therefore, the periodic region of the crystal indeed acts like a high-reflectivity mirror at this frequency.

4.2 Bloch Modes

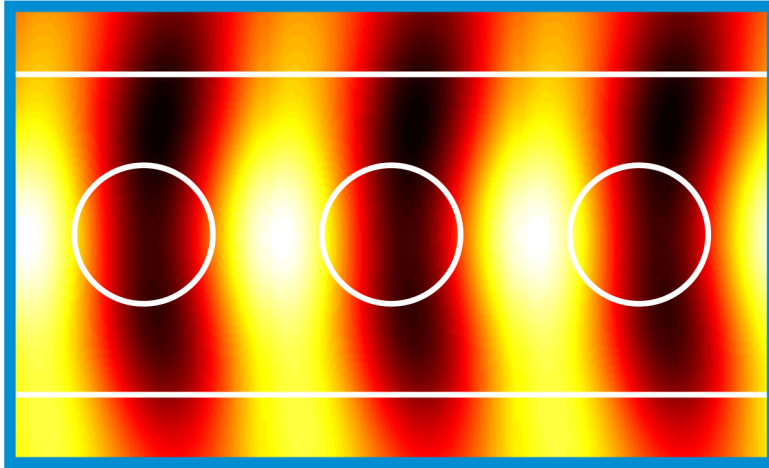


FIGURE 4.2: Simulated Bloch mode for $f_1 = 340.21$ THz marked with a blue polygon in the band structure graph. The white lines indicate the boundaries of the cavity and the holes. The white areas depict regions of high intensity. The dark areas mark regions of low intensity.

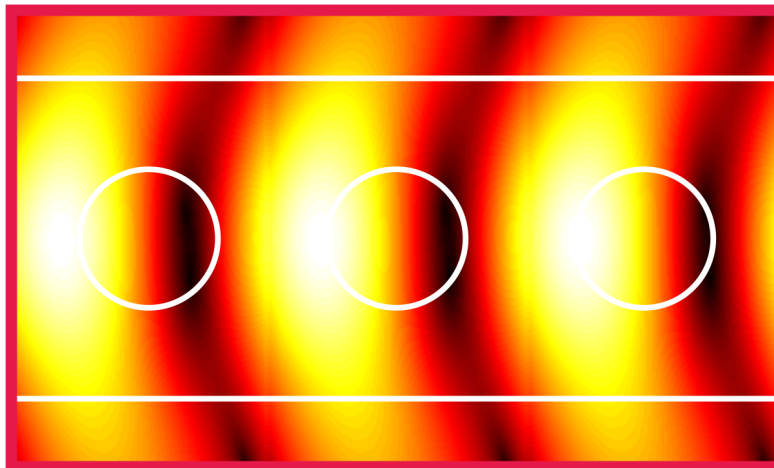


FIGURE 4.3: Simulated Bloch mode for $f_2 = 397.86$ THz marked with a pink polygon in the band structure graph. The white lines indicate the boundaries of the cavity and the holes. The white areas depict regions of high intensity. The dark areas mark regions of low intensity.

In the *Photonic Crystals* chapter, the origin of Bloch modes due to the discrete translational symmetry in PhCs was discussed. In figures 4.2 and 4.3 the Bloch modes at the frequencies $f_1 = 340.21$ THz to $f_2 = 397.86$ THz with $\mathbf{k}a = \pi$ marked with a polygon in the band structure graph are shown. The electric field intensity

is either more concentrated in the dielectric or rather pushed into the air while still obeying the imposed translational symmetry of the crystal.

4.3 Cavity Mode Profiles

If the periodicity of the one-dimensional PhC is broken up, a defect state in the PhC material is introduced and creates a PhC cavity. As described in the chapter *Photonic Crystals* decreasing the radius of individual holes pulls modes from the higher frequency air band down into the band gap. In order to get the best interaction of the rubidium atoms with the confined light, the set of modes concentrating their field in the air holes where the atoms can fly through has to be localized in the defect region. In the presented PhC cavity, the defect region is slowly tapered to a smaller hole size from the radius of the periodic region $r = 91$ nm to

$$r_4 = 81 \text{ nm},$$

$$r_3 = 73 \text{ nm},$$

$$r_2 = 67 \text{ nm},$$

$$r_1 = 63 \text{ nm}.$$

The distances between the positions of these holes are gradually decreased by $\Delta a = 1$ nm. Moreover, the distance between the first hole of the mirror region and the last hole of the tapered region is set to $a = 317$ nm in order to match the phase relation between the regions and to avoid scattering. As the defect region comprises a total of seven holes, there is some distributions of the electric field strength within this region. The intensities of the electric field are plotted against the x , y and z axis in figures 4.4, 4.5 and 4.6 and show how the electric field strength varies as a function of space. In figure 4.4 one can see the simulated electric field intensity profile $|E(x, y)|$. The top and side panels of the figures show horizontal and vertical cuts of the electric field through the center of the cavity. The white lines indicate the boundaries of the holes and the slab. The arrows corresponding to x and y mark the spatial orientation. One can observe in figure 4.4 that the electric field exhibits a maximum intensity in the central hole of the tapered region. The cross sections in figures 4.5 and 4.6 show the evanescent tails of the electric field along both the y and z direction. The cross section along the y -axis in figure 4.6 is especially interesting as one can clearly see how the electric field is really confined in the airy hole and suppressed in the dielectric region.

The resonance frequency λ_{Cav} of the cavity for a simulation mesh of $dx = dy = dz = 7$ nm is given by

$$\lambda_{\text{Cav}} = 781.83 \text{ nm.}$$

The resonance frequency of the cavity can shift by changing the mesh size and the simulation can be further optimized. For the given mesh size, the reported resonance frequency of the cavity still has a detuning of $\Delta = 1,59$ nm from the D_2 line of the rubidium atom.

The trend observed while refining the mesh size from 15 nm to 7 nm showed that the resonance wavelength of the cavity slightly shifted down by $\Delta\lambda \approx 2$ nm towards a smaller wavelength. Therefore, one possibility to improve the result might be a refined mesh of $dx = dy = dz = 1$ nm. Another approach suggests a slight change of the properties of the tapered region. In the follow up studies of this work, another cavity with a resonance wavelength at $\lambda_{\text{Cav}} = 779.56$ nm could be designed by changing the distances between the positions of the tapered holes by $\Delta a = 2$ nm instead of $\Delta a = 1$ nm.

The cavity quantum electrodynamics parameters of the presented cavity with a resonance wavelength of $\lambda_{\text{Cav}} = 781.83$ nm are shown in the next chapter.

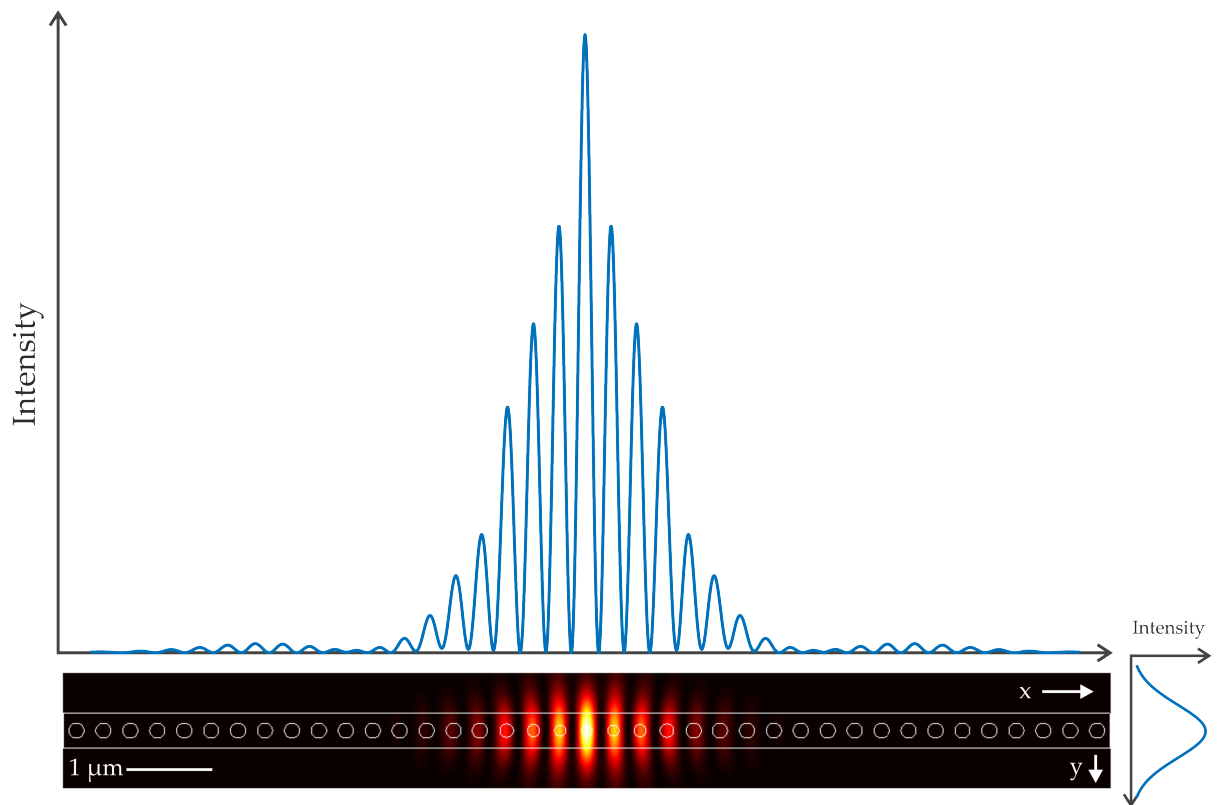


FIGURE 4.4: Simulated electric field intensity. The top and side panels show horizontal and vertical cuts of the electric field through the center of the cavity. The white lines indicate the boundaries of the cavity and the holes. The arrows corresponding to x and y mark the spatial orientation.

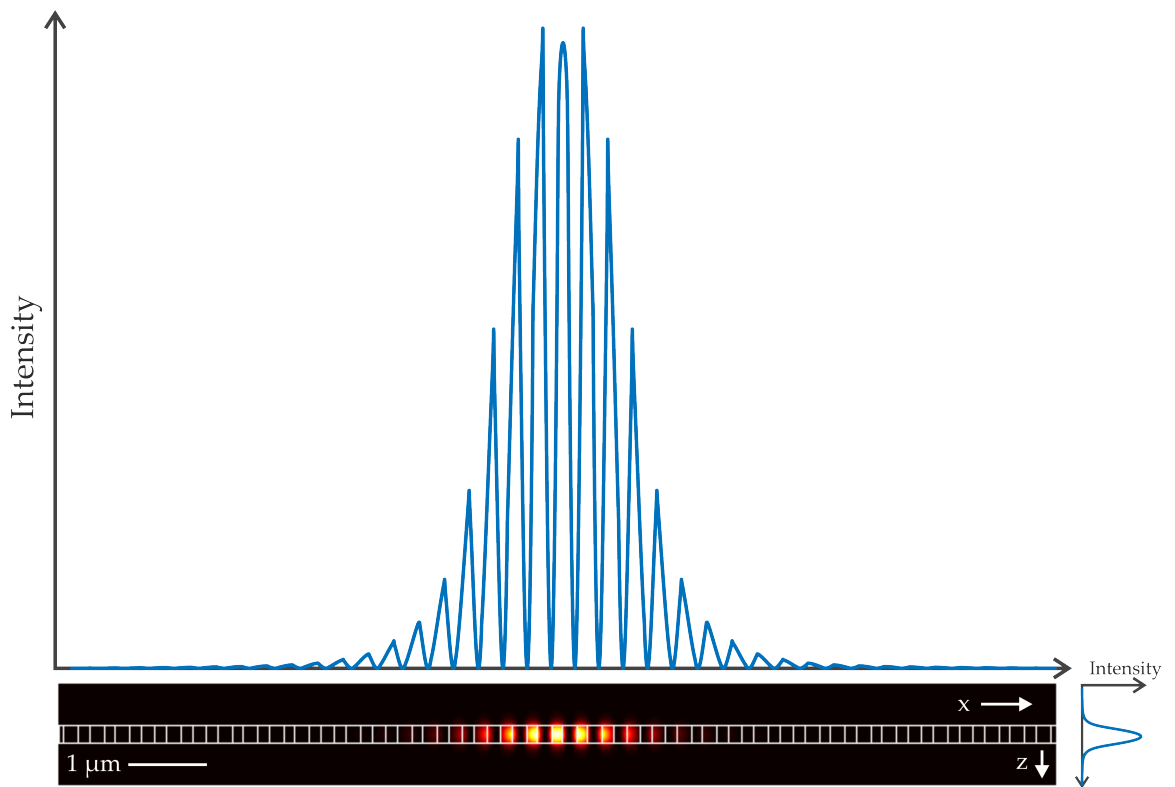


FIGURE 4.5: Simulated electric field intensity. The top and side panels show horizontal and vertical cuts of the electric field through the center of the cavity. The white lines indicate the boundaries of the cavity and the holes. The arrows corresponding to y and z mark the spatial orientation.

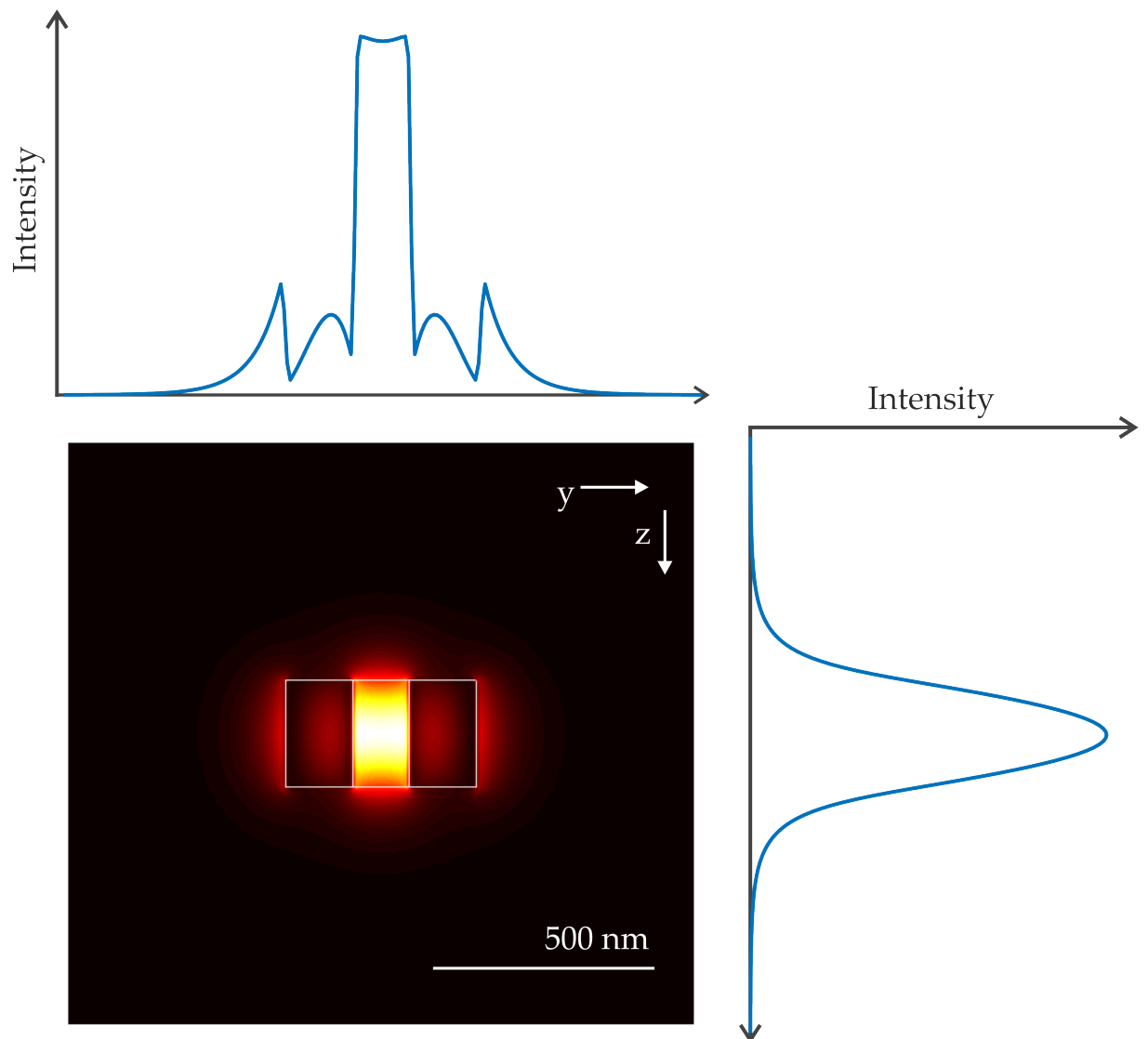


FIGURE 4.6: Simulated electric field intensity. The top and side panels show horizontal and vertical cuts of the electric field through the center of the cavity. The white lines indicate the boundaries of the cavity and the holes. The arrows corresponding to y and z mark the spatial orientation.

4.4 Cavity QED parameters

In the *Cavity Quantum Electrodynamics* chapter, the quality factor, mode volume, vacuum Rabi frequency and cooperativity have been introduced. The quality factor describing how long a photon stays in the cavity can be simply extracted out of

the FDTD simulation the same way as described in the theory. The mode volume V_m giving a measure of the spatial confinement of the electromagnetic field in the cavity can be calculated via equation (2.44) using the presented field profiles. The same applies to the calculation of the vacuum Rabi frequency via equation (2.45) giving the strength of the atom-photon interaction.

Only for the calculation of the cooperativity an approximation must be made. The cooperativity measures the ratio of the coherent and incoherent phenomena in a cQED system. It weighs the square of the atom-cavity coupling rate g against the unwanted loss mechanisms κ , the electric field decay, and $\Gamma_{0\perp}$, the atom's decay rate into non-resonant cavity modes which can be seen in equation (2.47).

The main loss channel $\Gamma_{0\perp}$ for hot atoms is caused by transit-time broadening. As the investigated atom is moving with a speed of $v = \sigma$ and is not trapped in the cavity, it is only experiencing the excitation of the light for a short time before leaving the defect region.

The atom is approximately moving with a speed of $v = 200$ m/s through the cavity with height, $h = 200$ nm, and experiences the electric field for only about 1 ns which in return leads to the approximation of the atom decay rate of $\Gamma_{0\perp} = 1$ GHz used in the cooperativity calculation.

As can be seen from the equation (2.47), increasing the figure of merit Q/V is critical in order to achieve high cooperativities.

For a simulation mesh of 7 nm, the cavity presented in this thesis has the simulated Quality factor Q , the decay rate κ , the mode volume V_m , the vacuum Rabi frequency g and cooperativity C of

$$\begin{aligned} Q &= 61,877, \\ \kappa &= 1.947 \cdot 10^{10}, \\ V_m &= 3.984 \cdot 10^{-20} \text{m}^3 = 0.0839 \cdot \lambda_0^3, \\ g &= 4.08 \cdot 10^{11} \text{ 1/s}, \\ C &= 4.28 \cdot 10^3. \end{aligned}$$

4.5 Temperature dependence of the PhC cavity

To get some information about the thermal behavior in the cavity, the effects of the thermal expansion and the change of the refractive index in the silicon nitride slab are taken into consideration. Therefore, the linear thermal expansion coefficient of silicon nitride [21]

$$\frac{dL}{dT} = 3.2 \cdot 10^{-6} 1/K$$

and the thermo-optic coefficient of silicon nitride [22]

$$\frac{dn}{dT} = 2.51 \pm 0.08 \cdot 10^{-5} 1/K$$

are used. The expansion coefficients are inserted into the equations,

$$L = L_0 + L_0 \cdot \frac{dL}{dT} \cdot \Delta T,$$

$$n = n_0 + n_0 \cdot \frac{dn}{dT} \cdot \Delta T$$

where L_0 and n_0 represent the initial length and the initial refractive index and ΔT the temperature change. Starting from 300 K the structure is simulated in steps of 50 degrees up to 350 K. The resonance wavelength and cooperativity as well as the quality factor and mode volume are plotted against these temperatures in figures 4.7 and 4.8 respectively. For each property a guide to the eye is connecting the simulated data points.

One can see how the resonance wavelength shifts up for approximately 3 nm towards larger wavelengths within the temperature interval of 250 degrees. The mode volume of the cavity decreases slightly and the quality factor increases due to the temperature change. The reasons for this trend are on the one hand, the increase of the refractive index leading to a better confinement and on the other hand, the new resonance wavelength for which the defect region acts like a better cavity. Although the figure of merit Q/V and thereby the cooperativity is increased via the temperature increase, the most important observation in these simulations is the shift of the resonance wavelength. Note, that the increasing cooperativity value does not improve the atom-light interaction in the cavity as long as the resonance wavelength of the cavity does not match the transition of the D_2 line.

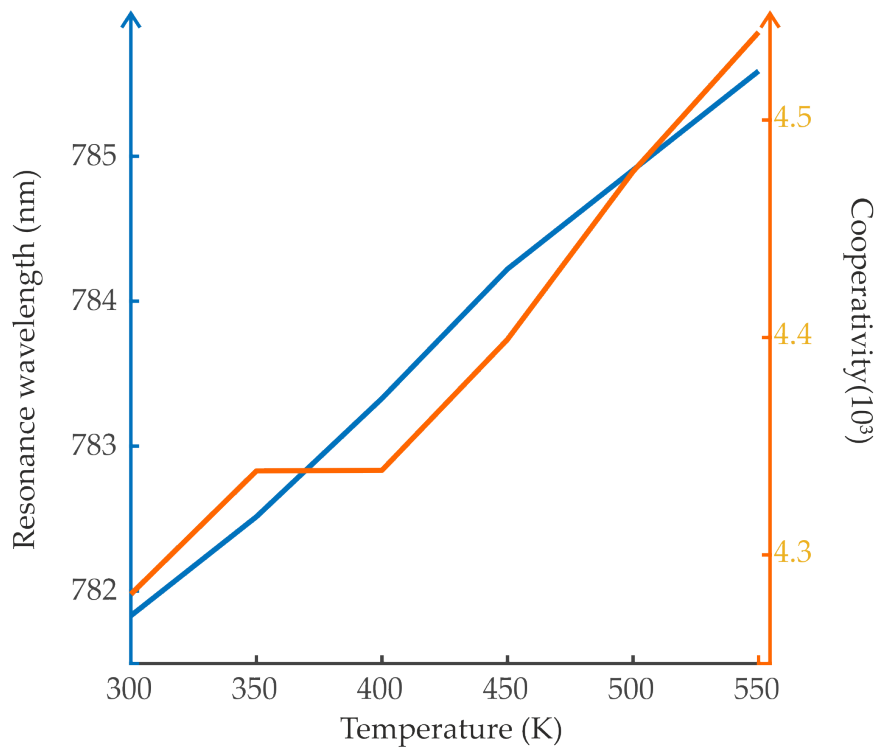


FIGURE 4.7: Temperature dependence of the resonance wavelength (blue) and cooperativity (orange) in the PhC cavity in a range from 300 to 550 K.

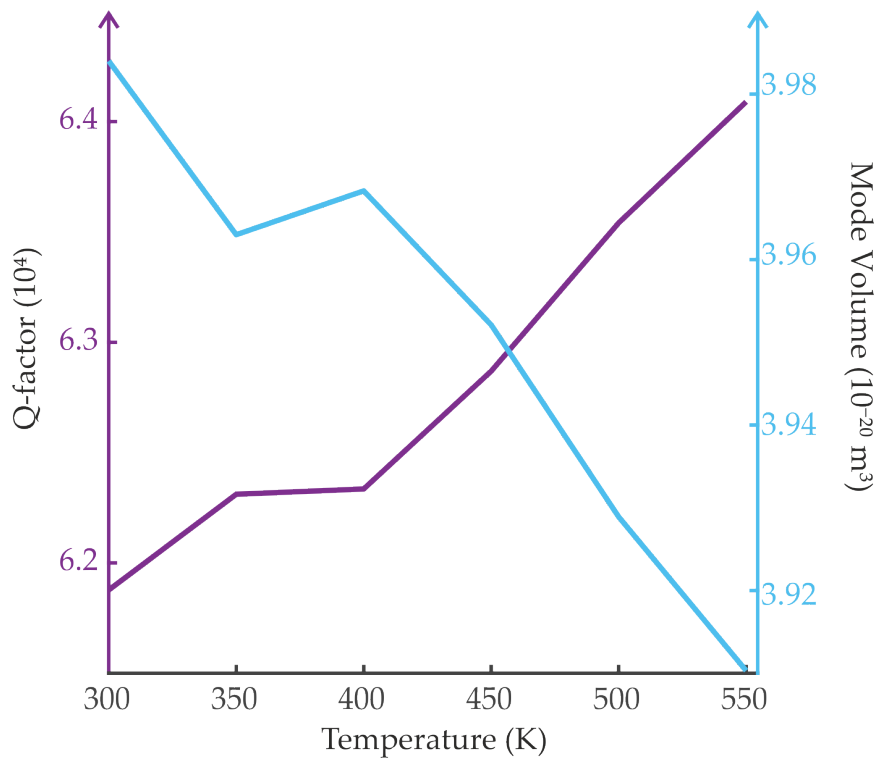


FIGURE 4.8: Temperature dependence of the Q-factor (purple) and mode volume (cyan) in the PhC cavity in a range from 300 to 550 K.

5 Outlook

The perfect, unperturbed interaction of a two-level atom flying straight through a resonant PhC cavity shows an idealized interaction scenario of an atom and can illustrate some physical effects within the cavity well. However, it is not directly applicable as a result to a real system of hot atoms where more parameters have to be taken into account in an investigation. That is why this analysis is moved to the outlook.

5.1 A Two-Level Atom coupled to the PhC Cavity

As discussed in the chapter *Atom-Light Interaction*, applying a resonant, electromagnetic field to a two-level atom leads to Rabi-Oscillations. After a certain time this oscillation exchanging the energy of a photon between the atom levels and the resonant cavity field is damped due to spontaneous emission of the atom and other effects. In order to still achieve a coherent Rabi oscillation, the coupling between the light and the electromagnetic field of the cavity must be strong enough.

In the outlook of this thesis, a simulation of an atom flying through the centered hole of the cavity is presented. Therefore the Matlab code described in the chapter *Basics of the Simulation* is used. The rubidium atom inserted into the simulation starts from an initial position on the top of the z -axis of the simulation region in its initial, unexcited ground state. The elements of the density matrix are set to $\rho_{gg}(t = 0) = 1$ and $\rho_{ee}(t = 0) = 0$. The atom moves with a velocity of $v_z = \sigma \approx 169.74$ m/s, which is the standard deviation of the Maxwell speed distribution, parallel to the z -axis right through the center of the middle hole of the cavity. The enhancement of the atom's spontaneous emission rate is not considered yet and the decay rate Γ is set to the natural line width $\Gamma_0 = 2\pi \cdot 6.065$ MHz [20]. The evaluated time in the simulation covers the time that the atom needs to pass the cavity once.

In figure 5.1, the z -position of such an atom is depicted. The dashed lines represent the cavity boundaries at $z = \pm 120.5$ nm. The light blue region marks the time

interval during which the atom passes through the cavity. At the time $t = 0.283/\Gamma_0$, the atom hits the lower boundary of the simulation region at $z = -650$ nm and gets reflected back towards the slab.

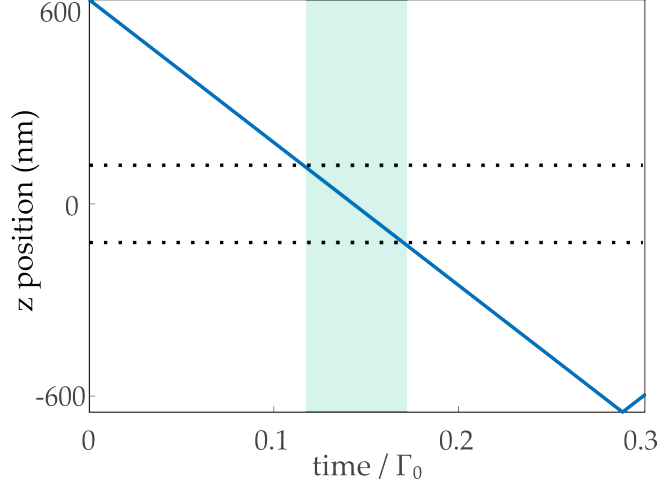


FIGURE 5.1: The z -position of the rubidium atom is depicted for 0.03 times the natural lifetime of the atom which equals the time that the atom with a velocity of $v_z = \sigma = 169.74$ m/s needs to pass the cavity once. The dashed lines represent the height of the cavity and the light blue region marks the period of time during which the atom passes the cavity.

As the atom passes the simulation region, it experiences different strengths of the electric field. Therefore the Rabi-frequency determined via equation (2.33) turns into a position-dependent quantity for the atom. The Rabi frequency of the atom becomes larger as the atom enters the strong electric field of the cavity as can be seen in figure 5.2 and reaches to its maximum right at the center of the slab.

As the electric field profiles from FDTD are derived from a computer simulation, their strength mainly depends on the initial conditions of the simulation. That is why the electric field distribution in the cavity is first normalized to its maximum value and then scaled by a factor $c = 10^5$ which leads to a total number of photons, $n_{\text{Ph}} = 0,27$ in the cavity. This is calculated through dividing the absolute energy in the cavity by the energy of a single photon $\hbar\omega_0$ with the radian frequency $\omega_0 = 2\pi f_{\text{D2}}$,

$$n_{\text{Ph}} = \frac{\int_V \frac{1}{2} \epsilon \epsilon_0 |E|^2 dV}{\hbar\omega_0}.$$

In figure 5.3 the population of the ground state ρ_{gg} of the atom flying through the cavity can be seen. As the atom enters the simulation in its ground state, the density matrix element ρ_{gg} is one in the beginning, the atom is completely in its

ground state and the coherence of the states is zero. As the atom flies through the field it starts interacting with the field and gets polarized. That means the population of the atom in the ground state decreases and its coherence increases. At $t \approx 0.08/\Gamma_0$ the atom is fully transferred to the excited state where both ρ_{gg} and $Im(\rho_{eg})$ vanish. As the atom gets closer to the slab the Rabi frequency increases (figure 5.2) hence the oscillations become faster (figure 5.3) . Due to the large coupling rate the atom goes through many Rabi flopping cycles before it leaves the hole which is depicted as the light blue region. Due to the spontaneous emission and the motion of the atom the oscillations are damped. After the atom leaves the hole, the Rabi frequency decreases due to the exponential decrease of the field leaking out of the cavity. This leads to slower oscillations and can be seen in both figure 5.3 and 5.4.

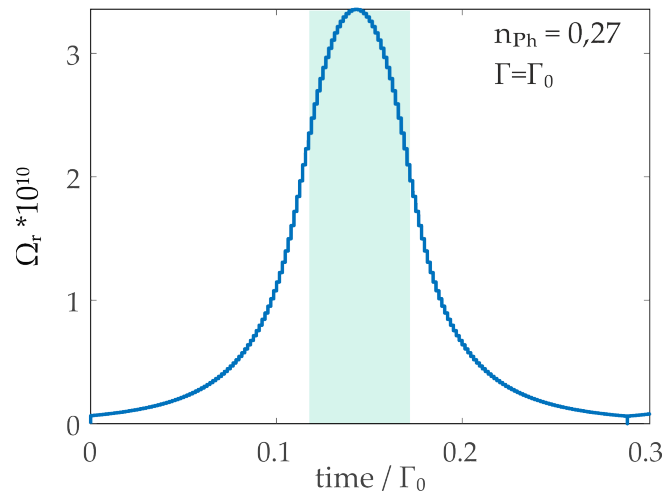


FIGURE 5.2: Time-dependent Rabi frequency Ω_r of the atom. The total number of photons in the cavity is $n_{\text{Ph}} = 0,27$. The decay rate of the atom is set to a constant value of $\Gamma = \Gamma_0$.

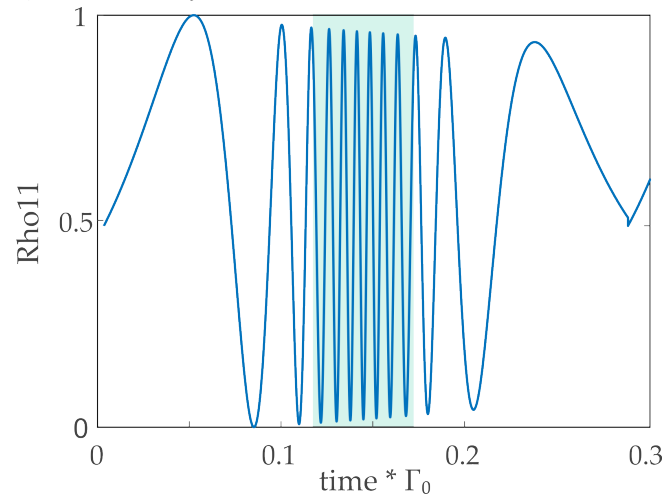


FIGURE 5.3: Time-dependent population of the ground state ρ_{gg} of the atom. The total number of photons in the cavity is $n_{\text{Ph}} = 0.27$. The decay rate of the atom is set to a constant value of $\Gamma = \Gamma_0$.

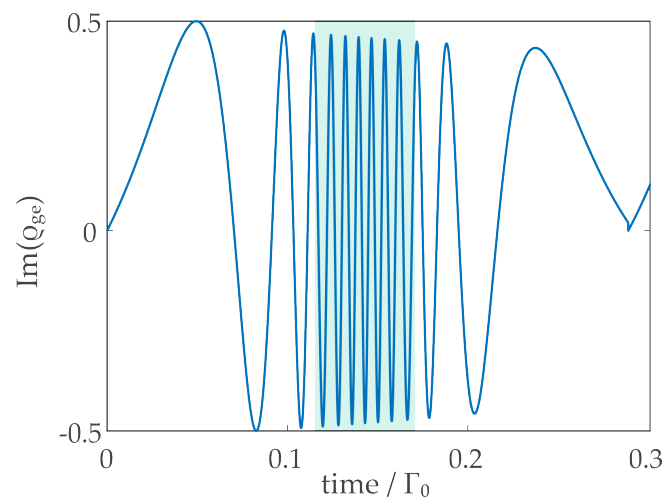


FIGURE 5.4: Time-dependent coherence $\text{Im}(\rho_{\text{gg}})$ of the atom. The total number of photons in the cavity is $n_{\text{Ph}} = 0,27$. The decay rate of the atom is set to a constant value of Γ_0 .

The perfect, unperturbed interaction of a two-level atom flying straight through the resonant light field of a PhC cavity is a good way to idealize the interaction of such an atom-cavity system and to illustrate the physical effect of the Rabi oscillation. However, for a real system many more parameters have to be taken into account. First, the effects of the Purcell factor must be taken into consideration. A single atom experiences an enhancement of its spontaneous emission rate by the Purcell factor. As the local density of states in the cavity increases, the atom receives more channels it can emit an absorbed photon to. As a result an atom absorbs and emits photons faster.

The decay rates into both kinds of modes, those supported by the cavity and those not supported by the cavity are enhanced. If the spontaneous emission into the cavity channels is enhanced, the Purcell effect is not representing a loss mechanism. But if the emission into a dissipative mode is heightened, the Purcell effect causes an increased loss of photons.

To separate these two effects, the desired and unwanted modes that the atom can emit to must be separated. Therefore, the symmetry boundary conditions in FDTD solutions are used and are enabled and disabled upon the cavity. With enabled symmetry boundaries, only the desired modes with the same symmetry as the cavity are isolated in the simulation and the enhancement of spontaneous emission into these modes is examined.

Without symmetry boundary conditions, all of the modes in the environment of the cavity are addressed by the atom and the total Purcell factor, i.e. the enhancement of spontaneous emission into all the modes is taken into account.

Subtracting those two Purcell factors leads to the value of the Purcell factor for the unwanted non-cavity modes $F_{P\perp}$ and thereby to the decay rate into dissipative channels $\Gamma_{0\perp} = F_{P\perp}\Gamma_0$.

Via the Purcell factor calculation described in the chapter *Basics of the Simulation*, a first total Purcell factor of

$$F_P = 7,314$$

for the dipole source placed right at the center of the cavity was calculated. The symmetry boundaries were disabled, the mesh size of the simulation was set to $dx = dy = dz = 15$ nm and the time of the simulation to $t = 100,000$ fs to have the fields fully decayed at the end of the simulation time.

For the same position of the dipole source, the symmetry boundary conditions were imposed on the simulation to have solely the desired modes with the same symmetry as the cavity isolated in the simulation. The calculated value of the Purcell factor however, represented an unphysical solution as its value was larger than the simulated total Purcell factor.

The reason for this lies in the properties of the boundary conditions. The symmetry boundaries act as a mirror for the dipole and double, quadruple or increase the power of the dipole source by eight. That is why for a representative value of the Purcell factor requires further simulations with a *transmission box* to normalize the power emitted by the dipole in the environment of the cavity to one single dipole. Moreover, several simulations with different orientations, i.e polarizations of the dipole source must be employed to couple to all the possible modes.

In addition, the dipole source must be spatially translated throughout the cavity to receive Purcell factors at different positions. Then a map of modified emission rates can be included into the Matlab analysis.

Furthermore, a real system requires a statistical description of an atomic ensemble with atoms following the Boltzmann velocity distribution. These atoms must have different velocity components in each spatial direction. This investigation will be the immediate follow up study of this thesis.

Finally, to inject and extract photons from this cavity, an input and output coupler at both sides of the cavity is needed. For that a design of an adiabatically tapered waveguide connecting the periodic mirror regions at both sides of the cavity to optical fibers is proposed. These regions with a gradual change from an optical fiber to a PhC region allow the optimal coupling of the light from optical fibers to the cavity and vice versa. The following figure shows a schematics of a similar, linear silicon-on-insulator waveguide taper device [23].

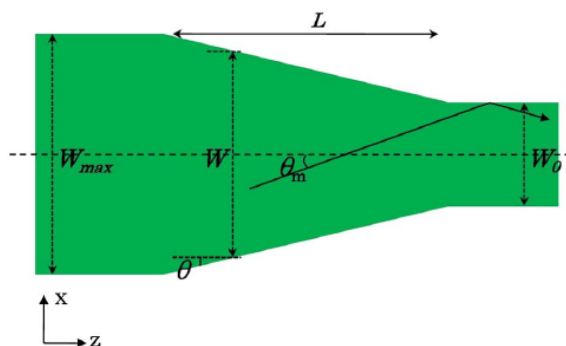


FIGURE 5.5: Schematics of the top view of a linear waveguide taper [23]. W_0 is the width of a single-mode waveguide, W_{\max} is the maximum taper width, L is the length of the taper, θ is the local half angle of the taper at point z , θ_m is the projection of the ray angle of the first-order mode of the taper [23]. For coupling the PhC cavity a similar adiabatically tapered device connecting the periodic mirror regions with width W_{\max} to optical fibers with diameter W_0 instead of waveguides is proposed.

6 Conclusion

The aim of this thesis was to design a nano-photonic crystal cavity resonating with rubidium atoms at $\lambda_{D2} = 780.24$ nm. For this purpose a design of a seven-hole tapered photonic crystal cavity within a silicon-nitride (Si_3N_4) slab was proposed. The presented design has a unit cell with the periodicity $a = 325$ nm, the radius of the holes $r = 91$ nm, the width of the cell $w = 426$ nm and the height $h = 241$ nm. The radii of the holes in the tapered region are decreased from $r = 91$ nm to $r_4 = 81$ nm, $r_3 = 73$ nm, $r_2 = 67$ nm and $r_1 = 63$ nm.

The distances between the positions of these holes are gradually decreased by $\Delta a = 1$ nm. Moreover, the distance between the first hole of the mirror region and the last hole of the tapered region is set to $a = 317$ nm in order to match the phase relation between the regions and to avoid scattering.

The resonance wavelength of the cavity λ_{Cav} for a simulation mesh of $dx = dy = dz = 7$ nm is given by $\lambda_{Cav} = 781.83$ nm. In the follow up studies of this work, another cavity with a resonance wavelength at $\lambda_{Cav} = 779.56$ nm could be designed by changing the distances between the positions of the tapered holes by $\Delta a = 2$ nm instead of $\Delta a = 1$ nm.

Nevertheless, the presented design still offers a good starting point for the investigations of the dimensions of the cavity quantum electrodynamics parameters in such a PhC cavity. It has the simulated Quality factor of $Q = 61,877$, the decay rate $\kappa = 1.947 \cdot 10^{10}$, the mode volume $V_m = 3.984 \cdot 10^{-20} \text{m}^3 = 0.0839 \cdot \lambda_0^3$, the vacuum Rabi frequency $g = 4.08 \cdot 10^{11}$ 1/s and the cooperativity $C = 4.28 \cdot 10^3$.

The Purcell factor for the dipole source right at the center of the cavity is given by $F_P = 7,314$ based on a mesh of $dx = dy = dz = 15$ nm and the time of the simulation $t = 100,000$ fs in FDTD. In order to receive the fraction of the Purcell factor enhancing the emission into non-cavity modes, the separation of the cavity and non-cavity modes is currently in progress.

In addition, instead of the presented idealized interaction of an atom moving through the resonant cavity, a statistical description of an atomic ensemble of atoms resonating with the light field will be part of the follow-up studies.

Bibliography

- [1] Mughees Khan, Thomas Babinec, Murray W. McCutcheon, Parag Deotare, and Marko Loncar. Fabrication and characterization of high-quality-factor silicon nitride nanobeam cavities. *Optics Letters*, 36(3), 2011.
- [2] John D. Joannopoulos, Steven G. Johnson, Joshua N. Winn, and Robert D. Meade. *Photonic Crystals: Molding the Flow of Light*. Princeton University Press, Princeton New Jersey, second edition, 2008.
- [3] C-L Hung et al. Trapped atoms in one-dimensional photonic crystals. *New Journal of Physics*, 15(083026), 2013.
- [4] Hans Lüth Harald Ibach. *Festkörperphysik, Einführung in die Grundlagen*. Springer-Verlag, Berlin Heidelberg, 2009.
- [5] Fritz Haber Institute of the Max Planck Society. Bloch theorem. [/www.fhi-berlin.mpg.de/~wolf/femtoweb/teaching/energybands_1_2.pdf](http://www.fhi-berlin.mpg.de/~wolf/femtoweb/teaching/energybands_1_2.pdf).
- [6] Jelena Vuckovic. Quantum optics and cavity qed with quantum dots in photonic crystals. *Oxford University Press*, 2013.
- [7] Robert Bettles. *Cooperative Interactions in Lattices of Atomic Dipoles*. Springer Theses, 6330 Cham, Switzerland, 2017.
- [8] Ralf Ritter. *Interfacing Thermal Atoms with Integrated Photonic Waveguides*. PhD thesis, Universität Stuttgart, 2018.
- [9] Massachusetts Institute of Technology. Chapter 2, maxwell bloch equations. <https://ocw.mit.edu/courses/electrical-engineering-and-computer-science/6-977-ultrafast-optics-spring-2005/lecture-notes/chapter2.pdf>.
- [10] M.H. Tooley. *Electronic Circuits: Fundamentals and Applications*. Butterworth-Heinemann, Linacre House, Jordan Hill, Oxford, 2006.

- [11] Philip Trost Kristensen, Cole Van Vlack, and Stephen Hughe. Effective mode volumes and purcell factors for leaky optical cavities. *Cornell University Library*, 2011.
- [12] Lumerical. Fdtd solver physics. https://kb.lumerical.com/en/solvers_finite_difference_time_domain.html. last visited on 2018-08-14.
- [13] Lumerical. Fdtd numerical methods. https://www.lumerical.com/support/courses/fdtd_numerical_methods/video.html.
- [14] Lumerical. Fdtd introductory webinar video. https://www.lumerical.com/support/courses/fdtd_introductory_webinar_video.html.
- [15] Lumerical. Fdtd bandstructure simulation methodology. https://kb.lumerical.com/en/diffractive_optics_pc_simulation_methodology.html. last visited on 2018-08-14.
- [16] Lumerical. 3d pc cavity analysis, simulation setup. https://kb.lumerical.com/en/diffractive_optics_pc_3d_cavity_setup.html. last visited on 2018-08-14.
- [17] Lumerical. Fdtd pcell factor. https://kb.lumerical.com/en/diffractive_optics_cavity_purcell_factor.html. last visited on 2018-08-14.
- [18] Lumerical. Fdtd tips for simulating high q photonic crystal and phc-cavity. <https://kx.lumerical.com/t/tips-for-simulating-high-q-photonic-crystal-phc-cavity/357>. last visited on 2018-08-14.
- [19] HU Berlin. Fourth order runge-kutta. <http://lpsa.swarthmore.edu/NumInt/NumIntFourth.html>. last visited on 2018-08-15.
- [20] Daniel A. Steck. Rubidium 87 d line data.
- [21] BYU Electrical and Computer Engineering. Coefficient of thermal expansion. http://cleanroom.byu.edu/CTE_materials. last visited on 2018-07-23.
- [22] Ali W. Elshaari et al. Thermo-optic characterization of silicon nitride resonators for cryogenic photonic circuits. *IEEE Photonics Journal*, 8.
- [23] Yunfei Fu, Tong Ye, Weijie Tang, and Tao Chu. Efficient adiabatic silicon-on-insulator waveguide taper. *OSA Publishing*, 2(3), 2014.

Acknowledgements

At the end of this thesis, I would like to thank those who have supported me during my time at the 5th Physical Institute.

First of all, I would like to thank **Prof. Dr. Tilman Pfau** for giving me the kind opportunity of writing my Bachelor thesis at the 5th Physical Institute.

Special thanks to **Dr. Hadiseh Alaeian** who has always encouraged me and taken her time to answer my endless questions. Thank you for your patience, teaching me atomic physics and how to work scientifically.

Thanks to **Dr. Hadiseh Alaeian, Dr. Harald Kübler, Artur Skljarow** and **Patrick Kaspar** for reading through my thesis and improving it with every little comment.

Thanks to **Dr. Robert Löw** for awakening my interest in the linear optics lecture.

I thank **Artur Skljarow** and **Markus Fiedler** for their great willingness to help me with Matlab problems and the nice time together at the office.

Thanks to my fellow student **Izel Gediz** for helping me through the hard times and being my super cool partner at the lab course.

Thanks to my family and friends who have supported me during my studies.

Finally, thanks to **Elmedin** who has had to back down during my time writing the thesis. Thanks for always cheering me up.